LA-UR-20-28111 (Accepted Manuscript)

Simultaneous Observations of Electromagnetic Ion Cyclotron (EMIC) Waves and Pitch Angle Scattering During a Van Allen Probes Conjunction

Sigsbee, K.
Kletzing, C. A.
Faden, J. B.
Jaynes, A. N.
Reeves, Edmond Geoffrey David
Jahn, J. M.

To be published in: Journal of Geophysical Research: Space Physics

DOI to publisher's version: 10.1029/2019JA027424

Permalink to record: http://permalink.lanl.gov/object/view?what=info:lanl-repo/lareport/LA-UR-20-28111

Simultaneous observations of electromagnetic ion cyclotron (EMIC) waves and pitch angle scattering during a Van Allen Probes conjunction

K. Sigsbee[1], C. A. Kletzing[1], J. Faden[1], A. N. Jaynes[1], Geoff Reeves[2], and J.-M. Jahn[3]

[1]Department of Physics and Astronomy, University of Iowa, Iowa City, Iowa, USA

[2]Space and Atmospheric Sciences, NIS-1, Los Alamos National Laboratory, Los Alamos, New Mexico, USA

[3]Southwest Research Institute, San Antonio, TX

Corresponding Author: K. Sigsbee, Department of Physics and Astronomy, University of Iowa, Iowa City, IA 52242, USA (kristine-sigsbee@uiowa.edu)

Key Points

Electromagnetic ion cyclotron waves generated by enhanced solar wind dynamic pressure were observed during the recovery phase of a storm.

Both of the Van Allen Probes observed electromagnetic ion cyclotron waves with similar spatial structure outside the dayside plasmapause.

Electromagnetic ion cyclotron waves with amplitudes up to 9 nT produced pitch angle scattering of > 10 keV protons and ~2 MeV electrons.

Plain Language Summary

In 1958, James Van Allen discovered Earth was surrounded by rings of electrons and ions, now called the radiation belts. In 2012, NASA launched the twin Van Allen Probes to study the radiation belts. Radiation belt electrons traveling near the speed of light can damage communication and weather satellites, and pose a risk to astronauts. Electromagnetic waves from 1-2 cycles every 10 minutes up to radio frequencies (several thousand cycles per second) are critical to radiation belt physics. Some waves energize the radiation belts, while others decrease their strength. We studied electromagnetic ion cyclotron (EMIC) waves (1-4 cycles per second) during a geomagnetic storm. The Van Allen Probes encountered two EMIC wave activity regions 25,000 km above Earth's surface, one just before local noon, and one slightly after local noon. The two satellites were close together and observed the waves in each region simultaneously. The wave activity regions were 2000-4000 km wide and 8000 km across (twice the distance from Washington, DC to San Francisco). Although this geomagnetic storm increased the global radiation belt strength, EMIC waves ejected electrons and protons from their paths around Earth, temporarily reducing the local radiation belt strength measured by the Van Allen Probes.

Abstract

On 22 December 2015, the Van Allen Probes observed two sets of electromagnetic ion cyclotron (EMIC) wave bursts during a close conjunction when Probe A and Probe B were separated by 0.57 to 0.68 R_E. The EMIC waves occurred during an active period in the recovery phase of a coronal mass ejection (CME) driven geomagnetic storm. Both spacecraft observed EMIC wave bursts that had similar spatial structure within a 1-2 minute time delay. The EMIC waves occurred outside the plasmasphere, within $\Delta L \approx 1\text{-}2$ R_E of the plasmapause and within a few degrees in magnetic latitude of the equatorial plane. The spatial structure of the EMIC waves appeared to be correlated with total magnetic field strength variations during solar wind pressure enhancements. The EMIC waves were observed in a narrow L shell region from $L \approx 4.55\text{-}5.32$ R_E between 10-11 MLT on the outbound halves of the spacecraft orbits, and from $L \approx 4.82\text{-}5.51$ R_E between 13-14 MLT on the inbound halves of the spacecraft orbits. The anisotropy of the proton pitch angle distributions was enhanced when the EMIC waves were observed. Although the overall radiation belt response during this storm was dominated by acceleration and transport processes, the EMIC waves produced local pitch angle scattering of 13-15 keV protons and 2.1-2.6 MeV electrons.

Index Terms:

2774 Radiation belts, 2788 Magnetic storms and substorms, 2772 Plasma waves and instabilities, 7867 Wave/particle interactions, 2784 Solar wind/magnetosphere interactions

Keywords: EMIC Waves, Plasmapause, Proton Anisotropy, Storm Recovery Phase, Van Allen Probes, Pitch Angle Scattering

1. Introduction

In satellite magnetic field observations, electromagnetic ion cyclotron (EMIC) waves are typically found in three frequency bands defined by the O^+, He^+, and H^+ ion gyrofrequencies [e.g., Kozyra et al., 1984; Gomberoff and Neira, 1983]. EMIC waves are of great interest to the magnetospheric physics community as they can contribute to radiation belt electron losses [e.g., Ukhorskiy et al., 2010; Meredith et al., 2003] and precipitation of ring current protons [e.g., Jordanova et al., 2001]. CRRES data have shown that for EMIC waves observed below ±11° magnetic latitude (MLAT), energy propagation can be bidirectional both toward and away from the magnetic equator, but for events located above ±11° MLAT, energy propagation is unidirectional away from the equator, suggesting a broad EMIC wave source region near the magnetic equator [Loto'aniu et al., 2005].

The earliest studies of EMIC wave growth considered cyclotron instabilities involving proton beams with anisotropic distributions and velocities greater than the phase velocity of the unstable wave, which in these theories is the Alfvén speed [Cornwall, 1965]. Some of these early papers even considered how EMIC waves should behave in multi-component plasmas [Cornwall and Schulz, 1971; Gomberoff and Neira, 1983]. In more recent papers, development of EMIC wave growth theories and models has often focused on convective growth rates and evolution of the ion temperature anisotropy [e.g., Kozyra et al., 1984; Horne and Thorne, 1994; Bortnik et al., 2011]. Many EMIC wave studies have demonstrated these waves are often associated with magnetospheric compressions [e.g., Usanova et al., 2010; Kim et al., 2017], which can increase the ion temperature anisotropy in the dayside magnetosphere [e.g., McCollough et al., 2010; 2012]. However, theory and modeling studies have also indicated that kappa type ion velocity distributions with power law tails [e.g., Mace et al., 2011], as well as ring-like ion pitch angle

93 distributions near the Alfvén speed, can enhance EMIC wave growth [Mithaiwala et al., 2013; Fok
94 et al., 2016; Min and Liu, 2016; Yu et al., 2018].

95 In this paper, we present a detailed case study analysis of a time interval when the two Van
96 Allen Probes were separated by 0.56 to 0.68 R_E and both spacecraft observed the same two sets of
97 H^+ band EMIC wave bursts. We will discuss these EMIC waves in context of the upstream solar
98 wind conditions and geomagnetic activity during the 19-22 December 2015 storm, and estimate
99 their spatial extent and location relative to the plasmapause. We will also examine the wave
100 amplitudes, proton anisotropies, pitch angle distributions, and plasma composition during these
101 EMIC wave observations.

102

103 **2. The Van Allen Probes Mission and Data Sets**

104 The Van Allen Probes (formerly known as the Radiation Belt Storm Probes, RBSP-A and
105 RBSP-B) were launched in 2012 into nearly identical orbits with ~10° inclinations and initial
106 perigees of 1.1 R_E and apogees of 5.8 R_E geocentric. The orbits of the Van Allen Probes were
107 designed so that the two spacecraft periodically lap one another as they orbit the Earth. The EMIC
108 wave case study presented here occurred 2 days after a spacecraft lapping event, when the two
109 Van Allen Probes were still close together. This paper will use data from the Electric and Magnetic
110 Field Instrument Suite and Integrated Science (EMFISIS) [Kletzing et al., 2013] tri-axial fluxgate
111 magnetometer (MAG) which measures DC to ~30 Hz magnetic fields to examine the EMIC waves.
112 Plasma wave data from EMFISIS will also be used to provide plasma densities based upon the
113 upper hybrid line [Kurth et al., 2015]. We will also examine proton temperature anisotropies and
114 the overall anisotropy of the proton pitch angle distributions as a function of energy using the Van
115 Allen Probes Helium, Oxygen, Proton, and Electron (HOPE) mass spectrometers [Funsten et al.,

116 2013] which are part of the Van Allen Probes Energetic Particle, Composition, and Thermal
117 Plasma (ECT) [Spence et al., 2013] instrument suite. HOPE provides data for electrons and ion
118 composition for energies between 0.9 eV above the spacecraft potential up to 50 keV. To examine
119 pitch angle scattering of relativistic electrons, we also used data from the ECT Magnetic Electron
120 Ion Spectrometer (MagEIS) [Blake et al., 2013] and the ECT Relativistic Electron-Proton
121 Telescope (REPT) Instrument [Baker et al., 2012].
122
123 **3. Space Weather Context for the EMIC Wave Observations**
124 According to the NOAA Space Weather Prediction Center (SWPC), the 19-22 December
125 2015 geomagnetic storm was caused by two Earth-directed, asymmetrical full-halo coronal mass
126 ejections (CMEs) that erupted on 16 December 2015. The first CME was observed in Solar and
127 Heliospheric Observatory (SOHO) Large Angle Spectroscopic Coronograph (LASCO) C2
128 imagery beginning at 09:24 UT on 16 December 2015 and was associated with a C-class flare
129 which peaked around 09:00 UT. The second CME was associated with a filament eruption, and
130 was first observed in coronagraph imagery at 14:36 UT on 16 December 2015. According the
131 NOAA SWPC, the two CMEs appeared to have merged in the interplanetary medium, impacting
132 the Earth at 15:28 UT on 19 December 2015. The flare and propagation of these CMEs have been
133 discussed in published papers [e.g., Liu et al., 2018; Balasis et al., 2018], but due to their unique
134 perspectives, these papers give slightly different accounts of the transits of these disturbances
135 through interplanetary space. As we are concerned with the resulting geomagnetic activity, we
136 will use the archived NOAA SWPC reports to establish a timeline for the 22 December 2015 EMIC
137 wave events in the context of the storm. The NOAA SWPC reported that during the passage of
138 the interplanetary shock, the ACE spacecraft measured an increase in the solar wind total magnetic

field from 5 nT to 17 nT. Shortly after the initial shock passage, the B_Z GSM component of the solar wind magnetic field turned strongly southward. A prolonged period of southward magnetic field ($-B_Z$) associated with the passage of the CMEs caused periods of geomagnetically active conditions late on 19 December 2015. The NOAA SWPC reported that active to moderate G2 geomagnetic storm conditions were observed from 03:00-06:00 UT on 20 December 2015 and from 15:00 UT on 20 December 2015 to 06:00 UT on 21 December 2015. The minimum Dst index during this storm was -155 nT at 22:00 UT on 20 December. G1 storm conditions occurred from 06:00-09:00 UT on 21 December 2015.

The 19-22 December 2015 storm was a significant and complex event that has been mentioned in several papers on the effects of space weather. These papers have examined the scintillation of transionospheric radio signals [Chashei et al., 2016; Loucks et al., 2017; Wang et al., 2018; Zakharenkova and Cherniak, 2018], the ionospheric total electron content (TEC) [Blagoveshchensky et al., 2018; Mansilla, 2019], geomagnetically induced currents (GIC) in the Irish power network [Blake et al., 2016], and the response of the magnetosphere as a non-linear system [Balasis et al., 2018]. This storm has also been mentioned in papers using Van Allen Probes data, including a study of impulsive electric fields associated with interplanetary shocks [Zhang et al., 2018], a study of whistler mode chorus with tones that oscillate in frequency [Gao et al., 2017], and a survey of radiation belt enhancements observed by the Van Allen Probes from October 2012 to April 2017 [Boyd et al., 2018].

The EMIC waves we will discuss in this paper occurred during the recovery phase of the 19-22 December 2015 storm in an isolated active period early on 22 December 2015 associated with an increase in solar wind dynamic pressure. Figure 1 shows an overview of the NASA OMNI upstream solar wind parameters [King and Papitashvili, 2005] that have been time-shifted to the

Earth's bow shock nose. The OMNI method of time-shifting upstream solar wind data to Earth takes into account the location of the observing spacecraft, the solar wind speed, and the speed of the Earth's orbital motion, while assuming the orientation of the phase front relative to the Earth-Sun line is half-way between the corotation geometry and convection geometry. From top to bottom, Figure 1 shows the OMNI solar wind speed, solar wind dynamic pressure, the B_Z GSM component of the interplanetary magnetic field, the 2.6 MeV omni-directional electron flux from the ECT REPT on Van Allen Probe A (RBSP-A) binned as a function L shell versus time, the Dst index, and Kp index. The OMNI solar wind plasma parameters were derived from Wind data during the time period shown in Figure 1 as the ACE data had gaps in coverage.

In Figure 1, a decrease in the 2.6 MeV RBSP-A REPT electron flux appears at the largest L shells at the beginning of 20 December 2015, and spreads to lower L shells, until roughly 19:00 UT when the fluxes begin to recover. A similar pattern appears also in the REPT electron fluxes at other energies up to 6.3 MeV, as well as in the MagEIS electron fluxes above 346 keV. Because this decrease in the electron fluxes closely tracks the Dst index and develops over a broad range of energies and across L shells, it may be due to the "Dst effect." The "Dst effect" is an observed decrease in the energetic electron fluxes resulting from the development of the storm-time ring current and associated decrease of the inner magnetosphere magnetic field strength [e.g., Li et al., 1997, Kim and Chan, 1997]. As the name implies, this effect produces decreases in the energetic electron fluxes that are strongly correlated with the decrease in the Dst index during the storm main phase. Figure 1 also shows that during the storm main phase, the solar wind dynamic pressure occasionally reached values greater than 20 nPa and prolonged southward interplanetary magnetic fields were observed. Upstream solar wind conditions like these can cause the last closed drift shell in the dayside magnetosphere to move earthward, resulting in permanent electron losses

185 over a broad range of energies from the outer regions of the radiation belts when particle drift paths
186 cross the magnetopause [e.g., Kim et al., 2008; 2010; Matsumura et al., 2011; Yu et al., 2013].
187 This process is known as magnetopause shadowing [West et al., 1972] and it is an irreversible,
188 non-adiabatic process. Thus, the electron flux dropout during main phase of this geomagnetic
189 storm on 20-21 December 2015 was most likely not due to EMIC waves, although several intervals
190 of EMIC waves were observed during this storm.

191 The two intervals of EMIC waves we will discuss in this paper are marked in Figure 1 with
192 vertical lines at 06:27-07:15 UT and 10:15-11:03 UT on 22 December 2015. The marked intervals
193 in Figure 1 have been labeled as "outbound" to indicate that the Van Allen Probes were traveling
194 out of the plasmasphere towards apogee when the first interval of EMIC waves was observed, and
195 "inbound" to indicate that the Van Allen Probes were heading back towards the plasmasphere
196 when the second interval of EMIC waves was observed. During each of the marked time intervals,
197 EMIC waves were observed simultaneously by both of the Van Allen Probes on the day side.
198 These EMIC waves were associated with brief solar wind dynamic pressure pulses that occurred
199 near the end of a longer solar wind dynamic pressure enhancement from 21:00 UT on 21 December
200 2015 to 11:50 UT on 22 December 2015.

201 Neither Wind nor ACE was located directly on the Earth-Sun line when they encountered
202 the solar wind dynamic pressure enhancements during the marked intervals in Figure 1, so we
203 compared data between these two spacecraft to estimate the spatial scale of the solar wind
204 structures related to the EMIC waves observed on 22 December 2015. The increases in solar wind
205 density and dynamic pressure associated with the outbound marked EMIC wave time interval in
206 Figure 1 were observed by Wind from about 05:52 to 06:32 UT on 22 December 2015, along with
207 a period of southward (negative B_Z GSM) magnetic field. ACE also began to observe a density

increase within a few minutes of Wind, but the ACE data have large gaps. However, ACE magnetic field data show variations in B_Z GSM similar to those observed by Wind, so it appears likely that both Wind and ACE encountered the same solar wind structure. At the start of the density increase around 05:52 UT, Wind was located at GSM (X,Y,Z)=(194.4, -19.5, -10.1) R_E and ACE was located at GSM (X,Y,Z)=(240.5,-9.2, 25.2) R_E. Although these density and dynamic pressure perturbations may seem small compared to those associated with the storm's onset and main phase on 19-20 December 2015, the relative positions of Wind and ACE indicate that this was actually a large structure capable of affecting the entire dayside magnetosphere. Due to gaps in the OMNI data it is difficult to determine exactly when this solar wind dynamic pressure enhancement reached Earth, but based upon Figure 1 it appears likely that it arrived a few minutes before the outbound interval of EMIC waves was observed on 22 December 2015.

The increases in solar wind density and dynamic pressure associated with the inbound set of EMIC wave bursts marked in Figure 1 were observed by Wind from about 09:27 to 10:14 UT. ACE also observed enhanced densities from about 09:11 to 10:14 UT. Both Wind and ACE observed a brief interval of northward (positive B_Z GSM) magnetic field followed by a longer period of southward magnetic field, with similar, but not completely identical structure. At 09:30 UT, while both upstream solar wind monitors were encountering this second region of increased density, Wind was located at GSM (X,Y,Z)=(194.3,-20.0,-7.8) R_E and ACE was located at GSM (X,Y,Z)=(240.5,-6.2,26.2) R_E. As before, it appears that this was a very large density structure, in spite of its short time duration in Figure 1. As shown in Figure 1, this solar wind dynamic pressure enhancement reached Earth around 10:10 UT on 22 December 2015 just a few minutes before the second interval of EMIC waves was observed.

Although several intervals of EMIC waves were observed throughout the 19-22 December 2015 geomagnetic storm, the overall, global behavior of the radiation belts during this storm appears to have been dominated by acceleration and transport processes [e.g., Boyd et al., 2018]. During this storm the Van Allen Probes EMFISIS observed intense chorus emissions [e.g., Gao et al., 2017], as well as strong Pc4-5 ultra-low frequency (ULF) waves, and significant equatorial noise (magnetosonic wave) activity. These waves have been shown by many studies to contribute to radiation belt enhancements [e.g. Horne and Thorne, 1998; Elkington et al., 1999; Horne et al., 2007; Takahashi and Ukhorskiy, 2007; Thorne et al., 2013]. As a result of the ongoing acceleration and transport processes during this storm, the 2.6 MeV electron fluxes observed by the Van Allen Probes REPT remained enhanced over a broad range of L shells throughout the time interval shown in Figure 1. According to the NOAA SWPC, the greater than 2 MeV electron flux at geosynchronous orbit was also at normal to high levels throughout the entire week of 21-27 December 2015. Even though the 16 December 2015 CMEs produced a geomagnetic storm that resulted in global enhancement of the radiation belts, the Van Allen Probes still observed evidence for local pitch angle scattering of electrons and protons by EMIC waves, which we will discuss in more detail later.

4. EMIC Wave Locations, Spatial Extent, and Amplitudes

Figure 2 shows the locations of the two Van Allen Probes on 22 December 2015 for the orbits when the two sets of simultaneous EMIC wave bursts were observed. For Van Allen Probe A (RBSP-A), this corresponds to orbit 3233, and for Van Allen Probe B (RBSP-B), this corresponds to orbit 3214. The top panel of Figure 2 shows the orbits of RBSP-A (red) and RBSP-B (blue) viewed looking down on the north pole as a function of L shell in R_E and magnetic local

253 time (MLT) in hours. The bottom panel of Figure 2 shows the orbits of RBSP-A and RBSP-B
254 viewed in the noon meridian as a function of L shell and magnetic latitude (MLAT) in degrees.
255 The two simultaneous intervals of EMIC wave bursts are marked with thick lines, and the start of
256 each EMIC wave interval is marked with a star. The arrows indicate the direction of motion on
257 the outbound and inbound halves of the satellite orbits. We determined the plasmapause locations
258 for RBSP-A orbit 3233 and RBSP-B orbit 3214 using the densities calculated from the EMFISIS
259 upper hybrid line [Kurth et al., 2015]. The locations of the outbound and inbound plasmapause
260 crossings for both spacecraft have been marked with green symbols in Figure 2. Table 1 gives the
261 locations and UT times of the outbound and inbound plasmapause observed by RBSP-A during
262 orbit 3233 and RBSP-B during orbit 3214. Table 2 and Table 3 give the times UT, locations, and
263 spacecraft separations of RBSP-A and RBSP-B during the two EMIC wave intervals we will
264 discuss in detail.

265 Figure 3 shows FFT spectrograms of the EMFISIS fluxgate magnetometer B_Y components
266 of the magnetic field in solar magnetic (SM) coordinates and a line plot of the total magnetic field.
267 The top panel shows data from RBSP-A for orbit 3233 and the bottom panel shows data from
268 RBSP-B for orbit 3214. The center panel shows the OMNI 1 minute solar wind dynamic pressure
269 shifted to the Earth's bow shock. In SM coordinates, the Z axis is parallel to the Earth's magnetic
270 dipole axis (positive North) and the Y axis is perpendicular to the plane containing the dipole axis
271 and the Earth-Sun line (positive in direction opposite to the Earth's orbital motion). Thus, the B_Y
272 SM component of the wave magnetic field should usually be perpendicular to the background
273 magnetic field in the inner magnetosphere. The He+ and H+ ion gyrofrequencies have been
274 overplotted with white lines, and indicate that these EMIC waves occurred in the proton (H+)
275 band. The FFTs were performed using a 1024-point sliding Hanning window with ¾ overlap

between windows. For 64 samples/s data, this corresponds to a 16 second FFT window that slides over by 4 seconds. Thus, the shortest time scale structure that can be resolved in the spectrogram is about 8-12 seconds in duration, or 2-3 overlapping FFT windows. The time intervals of the EMIC waves we will study in detail have been marked with vertical magenta lines in Figure 3.

The first set of EMIC wave bursts observed by both Van Allen Probes spacecraft on 22 December 2015 occurred on the outbound half of orbit 3233 for RBSP-A and orbit 3214 for RBSP-B between about 06:28 UT and 07:15 UT. As shown by Table 1, RBSP-A made an outbound plasmapause crossing near 9 MLT and L=3.48 at 05:35:49 UT. RBSP-B left the plasmasphere near 9 MLT and L=3.71 at 05:50:08 UT. An isolated EMIC wave burst was observed by RBSP-A just outside the plasmapause between 05:38 UT and 05:58 UT, but was not observed by RBSP-B, as shown by Figure 3. Our detailed analysis on the outbound halves of the Van Allen Probes' orbits will therefore focus on the set of EMIC waves starting at RBSP-A at 06:28:33 UT near 10.32 MLT and L=4.65 as shown in Table 2 and Figure 3. RBSP-B began to observe the same EMIC waves seen by RBSP-A at 06:28:54 UT near 10.0 MLT and L=4.55 as shown in Table 2 and Figure 3. During the outbound interval of EMIC waves, both spacecraft observed a set of four clearly separated EMIC wave bursts with similar durations and timing at both spacecraft. The times of the individual outbound wave bursts based upon RBSP-A data are marked with alternating light and dark grey boxes above each panel in Figure 3 and have been labeled 1-4. The durations of these 4 wave bursts ranged from 4-11 minutes and the spacings between the bursts ranged from 5-7 minutes. At the start of the outbound EMIC wave interval, the Van Allen Probes were separated by 0.57 R_E (about 3648 km) and about 0.3 hours MLT. At the conclusion of the outbound EMIC wave interval at 07:15 UT, the spacecraft were separated by 0.61 R_E (about 3900 km) and 0.4 hours MLT. Shortly after this time interval, RBSP-A observed another burst of EMIC waves

between 07:35 UT to 07:50 UT. RBSP-B also saw a very weak EMIC wave burst starting around 07:36 UT, but after a minute or two the wave power dropped close to the background level of the spectrograms in Figure 3.

To examine the amplitudes of the outbound set of EMIC wave bursts in more detail, we computed the magnetic field magnitude in the X-Y SM plane and detrended the data by subtracting a 30 second running average to remove the background magnetic field and lower frequency fluctuations. The Z axis in SM coordinates is aligned with the Earth's magnetic dipole axis, and therefore the wave magnetic field in the X-Y SM plane should be approximately perpendicular to the Earth's dipole magnetic field. The peak EMIC wave magnetic field amplitudes measured by RBSP-A during the outbound set of wave bursts were 0.9 nT, 1.8 nT, 6.5 nT, and 2.3 nT. The peak EMIC wave magnetic field amplitudes measured by RBSP-B during each of the outbound wave bursts were 5.1 nT, 11.4 nT, 12.0 nT, and 0.8 nT. The spectrograms in Figure 3 also show that RBSP-A observed the largest amplitude waves on the outbound half of orbit 3233 during the third and fourth EMIC wave bursts and that RBSP-B observed the largest amplitude waves on the outbound half of orbit 3214 during the second and third EMIC wave bursts. RBSP-B was located slightly closer to the equatorial plane than RBSP-A during the outbound set of EMIC wave bursts as shown by Table 2.

We subtracted the Olson-Pfitzer 1977 Quiet (OP77Q) magnetic field model [Olson and Pfitzer, 1982] from the observed magnetic field and determined the size of the perturbations during the solar wind dynamic pressure increases. On the outbound halves of the Van Allen Probes' orbits, the peak solar wind dynamic pressure values of about 9 nPa were associated with increases on the order of 15-20 nT in the local magnetic field magnitude measured by the Van Allen Probes. The gaps in the solar wind dynamic pressure make it difficult to determine if this parameter has a

strong effect on the wave power. However, if the EMIC wave power was controlled solely by the solar wind dynamic pressure, we would expect the wave power and wave amplitudes at RBSP-A and RBSP-B to vary in a similar manner, but they do not. Although the occurrence of the outbound interval of EMIC waves appears to be well-correlated with the increase in solar wind dynamic pressure and the magnetospheric compression, the variations in the wave power do not appear to strongly correlated with the solar wind dynamic pressure, as shown by Figure 3. The variations in wave amplitudes and power during the outbound EMIC wave interval may simply indicate that one spacecraft was located closer to the generation region than the other during each wave burst.

On the inbound half of orbit 3214, RBSP-B observed a weak EMIC wave burst from about 09:43 UT to 09:48 UT that appeared to be associated with a small increase in the solar wind dynamic pressure as shown by Figure 3. These waves were not observed by RBSP-A and will not be discussed in detail.

The second set of four simultaneous EMIC wave bursts occurred on the inbound half of RBSP-A orbit 3233 and RBSP-B orbit 3214 between 10:16 UT to 11:02 UT, about 3 hours UT after the first set of simultaneous EMIC wave bursts. During the second set of wave bursts RBSP-A and RBSP-B were separated by about 0.68 R_E (4352 km) and 0.44-0.48 hours MLT. As shown by Figure 3, the structure of the inbound set of EMIC wave bursts is clearly correlated with variations in the total magnetic field (as indicated by fluctuations of the ion gyrofrequencies) caused by large variations in the solar wind dynamic pressure. On the inbound halves of the Van Allen Probes' orbits, there were four closely connected wave bursts instead of four clearly separated bursts as on the outbound halves of the satellites' orbits. In spite of this key difference, it is remarkable that the structure of the EMIC wave bursts on both the outbound and inbound halves of the Van Allen Probes' orbits are so similar at both spacecraft. It is difficult to precisely

split the EMIC waves observed on the inbound halves of the Van Allen Probes' orbits into separate bursts due to their connectedness. Using the variations in magnetic field wave power with frequency in the B_Y SM spectrograms shown in Figure 3, along with the variations in the perpendicular magnetic field waveform amplitudes as a guide, we estimated that the durations of these four wave bursts ranged from 9-14 minutes. The times of the individual inbound wave bursts based upon RBSP-A data are marked with alternating light and dark grey boxes above each panel in Figure 3 and have been labeled 5-8.

To examine the wave amplitudes during the inbound set of EMIC wave bursts in detail, we once again computed the magnetic field magnitude in the X-Y SM plane and detrended the data by subtracting a 30 second running average. The peak EMIC wave magnetic field amplitudes measured by RBSP-A during each of the inbound wave bursts were 9.0 nT, 6.9 nT, 1.6 nT, and 1.9 nT. The peak EMIC wave magnetic field amplitudes measured by RBSP-B during the inbound set of wave bursts were 4.2 nT, 3.3 nT, 6.5 nT, and 3.2 nT. This can be seen in the spectrograms in Figure 3, which show RBSP-A observed the largest amplitude waves on the inbound half of orbit 3233 during the fifth and sixth EMIC wave bursts. RBSP-B observed slightly larger amplitude waves on the inbound half of orbit 3214 during the seventh EMIC wave burst, but the amplitudes of the four bursts were quite similar at RBSP-B. It is interesting to note that both spacecraft were located at higher latitudes in the southern hemisphere on the inbound halves of their orbits than on the outbound halves of their orbits, as shown by Table 3. Although relatively large amplitude EMIC waves were observed by both spacecraft on the inbound halves of their orbits, the largest amplitudes were a few nT smaller than on the outbound halves of the satellites' orbits. However, the EMIC wave activity was more sustained and less bursty on the inbound halves of the satellites' orbits than on the outbound halves. Comparison between the peak

amplitudes observed by the lead spacecraft with the second spacecraft on both the inbound and outbound passes does not show a consistent pattern that would indicate the waves are either growing or being damped throughout the entire region of wave activity. It seems likely that the amplitude variations in each of the EMIC wave bursts are the result of variations in the local particle populations generating the waves, even though the spatial structure of the regions of wave activity at both spacecraft and on the inbound and outbound halves of the orbits are similar. Although there are local, temporal variations in the EMIC wave amplitudes during each burst, the similarities in the overall spatial structure of the wave bursts suggests that there was persistent dayside EMIC wave activity for at least 4.5 hours UT over a region that was radially narrow, but covered a wide range in MLT. We will discuss this further in Section 9.1. After observing the inbound group of EMIC wave bursts, RBSP-A re-entered the plasmasphere first, near 15.46 MLT and L=3.4 as shown by Table 1. RBSP-B re-entered the plasmasphere 11 minutes after RBSP-A, near 15.11 MLT and L=3.38.

Throughout the inbound halves of the Van Allen Probes' orbits, the background magnetic field magnitude measured by RBSP-A was consistently 15-35 nT larger than the background magnetic field RBSP-B. This general trend agrees reasonably well with the predictions of the OP77Q magnetic field model, and is most likely due to the differences in the magnetic latitudes of the spacecraft, not the magnetospheric compressions. On the inbound halves of the spacecraft orbits, the solar wind dynamic pressure reached values up to nearly 12 nPa, and the maximum change in magnetic field magnitude associated with the solar wind dynamic pressure was greater than 30 nT at both spacecraft. As during the outbound EMIC wave interval, the peaks in EMIC wave amplitudes and power occur at different times on each spacecraft. This provides further support for the idea that the wave amplitudes may be more strongly affected by local wave

391 generation processes than the solar wind dynamic pressure. However, during the inbound EMIC
392 wave interval, it appears that the solar wind dynamic pressure reached larger values and sustained
393 those values for longer periods of time. This may partially explain why the EMIC wave activity
394 consists of longer bursts during the inbound interval. The range of solar wind dynamic pressures
395 and background magnetic field perturbations observed during both the outbound and inbound
396 passes through the regions of EMIC wave activity are similar to those reported in other studies of
397 EMIC waves associated with magnetospheric compressions [e.g., Cho et al., 2016; McCullough
398 et al., 2010; Usanova et al., 2008]
399
400 **7. Proton Anisotropy**
401 We examined Van Allen Probes HOPE proton data to help us understand the plasma
402 conditions driving the EMIC waves during this time interval. Figure 4 shows an overview of Van
403 Allen Probe A EMFISIS magnetic field and HOPE proton data for orbit 3233. The top panel
404 shows an FFT spectrogram of the B_Y SM component of the magnetic field with the H+ and He+
405 gyrofrequencies overplotted in white for reference. As before, the times of the individual wave
406 bursts based upon RBSP-A data are marked with alternating light and dark grey boxes numbered
407 1-8 above each panel in Figure 4. The second panel shows the HOPE proton temperature
408 anisotropy $T_\perp/T_\parallel$ for protons with energies above 30 eV. The third panel shows the HOPE proton
409 anisotropy as a function of time and energy for proton energies between 1 keV and 50 keV, with
410 the Alfvén energy E_A overplotted in black. The Alfvén energy is the energy of a proton at the
411 Alfvén speed calculated using the EMFISIS densities from the upper hybrid line and the EMFISIS
412 4 second fluxgate magnetometer data. The proton anisotropy is only plotted when the total proton
413 flux at each energy is greater than 65,000 $s^{-1}cm^{-2}ster^{-1}keV^{-1}$ to insure a valid result. The bottom

two panels of Figure 4 show the parallel (mean of 4.5°, 18.0°, and 36.0° pitch angles) and perpendicular (90° pitch angle) HOPE proton fluxes, with the Alfvén energy overplotted in black. Figure 5 shows an overview of Van Allen Probe B magnetic field and HOPE proton data for orbit 3214 in the same format as Figure 4. We compare the energies of the anisotropic protons to the Alfvén energy in Figures 4 and 5, as the particle populations providing energy to drive the waves should have velocities greater than the wave phase velocities [e.g. Cornwall, 1965; Mithaiwala et al., 2013].

The proton anisotropies as a function of time and energy shown in the third panel of Figures 4 and 5 are different from the proton temperature anisotropies calculated using the HOPE plasma moments. The HOPE plasma moments integrate over all energies and pitch angles measured by the instrument to calculate temperatures and relative densities for the major ion species of the warm plasma population in the inner magnetosphere. As shown in the second panel of Figures 4 and 5, the proton temperature anisotropy was actually greater than 1 for the entire time interval shown on both spacecraft, even though EMIC waves were only observed for relatively short time periods during RBSP-A orbit 3233 and RBSP-B orbit 3214. Although EMIC wave growth is typically associated with ion temperature anisotropy, the EMIC wave growth during this event may actually have been produced by the anisotropy of protons within a specific energy range [e.g. Cho et al., 2016], and integrating over energy and pitch angles to obtain the parallel and perpendicular proton temperatures may obscure the particles driving the waves. Therefore, we used the full resolution HOPE energy and pitch angle distributions to calculate the ion anisotropy as a function of time and energy, which we defined as the difference between the parallel and perpendicular ion flux divided by the total of the parallel and perpendicular ion fluxes at each energy. On the color bar used in the third panels of Figures 4 and 5, negative proton anisotropy

values (blue) indicate perpendicular protons dominate the pitch angle distributions, while positive proton anisotropy values (red) indicate parallel protons are dominant.

An interesting feature of the proton anisotropy and proton fluxes shown in Figures 4 and 5 is that below the Alfvén energy, the proton anisotropy is mixed, and seems to fluctuate randomly between perpendicular and parallel values. Perpendicular protons tend to dominate above 20,000 eV throughout much of the time interval shown. However, for energies just above the Alfvén energy, the proton anisotropy seems to be more perpendicular when the EMIC waves were observed and more parallel at other times. On the outbound halves of the spacecraft orbits, during the first set of EMIC wave bursts, the proton flux appears to be mainly perpendicular from just above the Alfvén energy up to 50 keV, as indicated by the third and fifth panels of Figures 4 and 5. However, the bursty structure of the EMIC waves observed by both RBSP-A and RBSP-B on the outbound halves of the spacecraft orbits does not seem to be clearly correlated with any specific feature in the proton anisotropy.

When both spacecraft were close to apogee, two energy-dispersed peaks appeared in the parallel and perpendicular proton fluxes. One peak started around 08:00 UT and extended from about 20 keV down to the Alfvén energy, and the other peak started around 09:25 UT near the top of the HOPE energy range, indicating proton injections occurred. From 08:00 UT, until the arrival of the next solar wind dynamic pressure increase, the proton anisotropy of the newly injected ions just above the Alfvén energy is mainly dominated by parallel particles, as indicated by the third panels of Figures 4 and 5. When the solar wind dynamic pressure increase arrives, the proton anisotropy shown in Figures 4 and 5 suddenly becomes more perpendicular in a narrow band of energy just above the Alfvén energy up to about 20 keV. Strong EMIC waves were observed by both spacecraft at this time. When this band of perpendicular ions disappears around 11:00 UT,

460 the EMIC waves also stop. This suggests that the second set of EMIC waves was associated with
461 a sudden increase in the proton anisotropy due to the magnetospheric compression.

462 It is interesting to note that during the inbound set of EMIC wave bursts, the proton
463 temperature anisotropy $T_\perp/T_\parallel$ is actually slightly lower at both spacecraft than it was during the
464 outbound set of EMIC wave bursts. One key difference between the outbound and inbound halves
465 of RBSP-A orbit 3233 and RBSP-B orbit 3214 is the injection of fresh protons capable of driving
466 EMIC waves. In a study of EMIC waves associated with sudden magnetic field changes at
467 geosynchronous orbit using GOES 10, 11, and 12, Kim et al. [2017] concluded that
468 magnetospheric compressions would not generate EMIC waves without source particles. The
469 presence of freshly injected protons, combined with the increased solar wind dynamic pressure
470 may explain why the EMIC waves on the inbound halves of the Van Allen Probes' orbits were
471 more persistent than the bursty EMIC waves observed on the outbound halves of the spacecraft
472 orbits.

473 Magnetospheric compressions associated with high solar wind dynamic pressure are
474 thought to provide favorable conditions for EMIC wave growth by enhancing the ion temperature
475 anisotropy $T_\perp/T_\parallel$ needed to drive EMIC waves. Temperature anisotropies in warm plasmas can
476 arise from energizing processes that alter the temperature in the perpendicular direction, but they
477 can also be produced by non-energizing processes that reallocate energy between the perpendicular
478 and parallel directions while allowing the overall plasma temperature to remain constant [e.g.
479 McCollough et al., 2010; Usanova et al., 2016]. An example of an energizing process that results
480 in increased temperature anisotropy is inward radial transport of warm ions that preserves the first
481 adiabatic invariant (gyromotion) due to convection electric fields that provide perpendicular
482 energy [e.g. Summers et al., 1998]. An example of a non-energizing process that can generate ion

483 temperature anisotropies is conservation of the first (gyromotion) and second (bounce motion)
484 adiabatic invariants as particles drift from the nightside to the dayside, which leads to drift-shell
485 splitting. Drift-shell spitting can contribute to temperature anisotropies if the proton fluxes
486 decrease with increasing L shell, and the proton population spreads in L shell as a function of
487 equatorial pitch angle, with greater fluxes of higher pitch angle protons found at higher L shells on
488 the dayside. Another possible non-energizing process can occur when near-equatorial particles at
489 higher L shells execute their bounce motion entirely in one hemisphere due to off-equatorial
490 minimum magnetic field regions produced by significant distortions of the dipole magnetic field
491 [e.g., Shabansky, 1971].

492 During the time intervals studied here, the increases in solar wind dynamic pressure
493 resulted in significant perturbations of the background magnetic field measured at the Van Allen
494 Probes. As discussed in Section 4, on the inbound halves of the spacecraft orbits, when they were
495 at the highest latitudes on this orbit, and separated by the greatest latitude difference, the difference
496 in the background magnetic field magnitudes measured at RBSP-A and RBSP-B was consistent
497 with the OP77Q model predictions. In spite of the magnetic field perturbations resulting from the
498 magnetospheric compression, on both the outbound and inbound halves of the Van Allen Probes'
499 orbits, the spacecraft closer to the equator observed the smaller background magnetic field
500 magnitude. Thus, the comparison between the Olson-Pfitzer 1977 Quiet (OP77Q) magnetic field
501 model [Olson and Pfitzer, 1982] and the magnetic fields observed by the Van Allen Probes indicate
502 that the neither spacecraft encountered an off-equatorial minimum magnetic field region during
503 this event. As the greatest magnetic latitude reached by the Van Allen Probes was only -9.40°
504 (RBSP-A, inbound), it is unlikely that off equatorial minimum magnetic field regions or
505 Shabansky orbits played a significant part in generating proton anisotropy during this EMIC wave

506 event. However, drift-shell splitting, as well as processes involved in radial proton transport may
507 still have been important in generating both the overall proton temperature anisotropy as well as
508 the proton pitch angle distribution anisotropy at energies above the Alfvén speed.
509
510 **8. Pitch Angle Scattering of Protons and Electrons**
511 We also examined the proton and electron pitch angle distributions to look for evidence of
512 scattering by EMIC waves on 22 December 2015. Figure 6 shows an FFT spectrogram of the B_Y
513 SM magnetic field and time-pitch angle spectrograms of the HOPE proton fluxes from RBSP-A
514 orbit 3233 for protons with energies of 9.6 keV, 13.1 keV, 15.2 keV, and 20.7 keV. In Figure 6,
515 the individual EMIC wave bursts have once again been marked with alternating light and dark
516 grey boxes above each panel labeled 1-8, while vertical lines indicate the start and end of the
517 intervals of wave activity. Following the example of Usanova et al. [2014] we normalized the
518 HOPE proton fluxes to their values at 90° pitch angle, to make it easier to identify when protons
519 are being scattered. Thus, the flux at 90° pitch angle in Figure 6 is equal to 1 at all times shown,
520 and the color bar indicates the fluxes at other pitch angles relative to their value at 90°. To reduce
521 rapid time variations in the pitch angle distributions in Figure 6, and make it easier to see large
522 scale features, we smoothed them with a running boxcar average of 7 spacecraft spin periods.
523 Figure 7 is in the same format as Figure 6, only data from RBSP-B orbit 3214 are shown.
524 As shown in Figures 6 and 7, the proton fluxes at 9.6 keV appear to be lower overall on
525 both spacecraft during the outbound interval of EMIC waves, and increase dramatically after the
526 spacecraft have left this region of wave activity. This suggests that there may have been some
527 scattering of the 9.6 keV protons by the EMIC waves. On RBSP-B, Figure 7 shows that the 9.6
528 keV proton fluxes below 45° and above 135° pitch angle also appear to be slightly lower relative

529 the 90° fluxes than was observed by RBSP-A in Figure 6 during the outbound interval of EMIC
530 waves. This is not surprising as the EMIC waves observed by RBSP-B had slightly higher
531 amplitudes than those observed by RBSP-A on the outbound pass. However, the effects of the
532 EMIC waves on the protons during the outbound interval of waves may not be very pronounced
533 due to the bursty, intermittent nature of the EMIC waves and the presence strong ULF waves at
534 this time.

535 Evidence for scattering of protons by the EMIC waves is even stronger on the inbound
536 halves of the spacecraft orbits. During the inbound interval of EMIC waves, the proton fluxes at
537 13.1 keV below 45° and above 135° dramatically decrease on both spacecraft when the waves are
538 observed. The loss of protons at pitch angles below and above 90° degrees is even more
539 pronounced at 15.2 keV. However, at 9.6 keV and 20.7 keV, the overall pitch angle distributions
540 appear to remain mostly unchanged when the waves are observed. Protons with energies of 13.1
541 keV and 15.2 keV correspond to the energies just above the Alfvén energy on the inbound halves
542 of the orbits in Figures 4 and 5 that also showed a strong increase in the perpendicular proton
543 anisotropy. We also examined the HOPE helium pitch angle distributions, but the variations in
544 the He+ pitch angle distributions were not clearly correlated with the EMIC waves.

545 The strong energy dependence of the proton losses below 45° and above 135° pitch angles
546 during the inbound EMIC wave intervals suggests that the proton losses are due to scattering by
547 the EMIC waves. Indeed, the energy range of the protons affected by the EMIC waves in Figures
548 6 and 7 are consistent with other studies of the ring current and proton precipitation. Losses of
549 ring current ions can result from both collisional processes [Jordanova et al., 1996a] and wave-
550 particle interactions involving EMIC waves [Jordanova et al., 1996b]. Jordanova et al. [2001]
551 investigated sources of proton precipitation during the May 14-16, 1997, magnetic storm. They

552 simulated the evolution of ring current H+, He+, and O+ using a kinetic drift-loss model driven by
553 energetic ion fluxes measured at geosynchronous orbit and studied the excitation of EMIC waves
554 in the equatorial plane. Jordanova et al. [2001] found that the regions of maximum wave activity
555 corresponded reasonably well to satellite observations and that the most intense proton fluxes were
556 caused by plasma wave scattering. The Imager for Magnetopause-to-Aurora Global Exploration
557 (IMAGE) spacecraft presented evidence for transient dayside subauroral proton precipitation
558 caused by EMIC waves equatorward of the nominal auroral oval during the ~10 minute interval
559 immediately following a large solar wind pressure pulse [Fuselier et al., 2004]. The precipitation
560 consisted of protons with energies of a few 10s of keVs, was detached from the main auroral oval,
561 and the location mapped to the equatorial plane in the inner magnetosphere, in the region of the
562 ring current. Although plasma wave observations were not available, Fuselier et al. [2004]
563 established the connection between the proton aurora observations and EMIC waves through
564 calculation of the EMIC wave growth rates using particle data from the Los Alamos
565 geosynchronous spacecraft. Thus, it appears likely that the EMIC wave and proton observations
566 shown in Figures 6 and 7 represent a proton precipitation event similar to those studied by
567 Jordanova et al. [2001] and Fuselier et al. [2004].

568 The Van Allen Probes data from 22 December 2015 also show evidence for scattering of
569 radiation belt electrons by the EMIC waves. The top panel of Figure 8 (RBSP-A) and Figure 9
570 (RBSP-B) shows an FFT spectrogram of the BY SM magnetic field with the H+ and He+ ion
571 gyrofrequencies in white, along with MagEIS and REPT electron data. The second panel of Figure
572 8 and Figure 9 shows pitch angle distributions from the MagEIS 1.1 MeV (RBSP-A) and 1.1 MeV
573 (RBSP-B) electron fluxes. The next four panels of Figure 8 and Figure 9 show pitch angle
574 distributions for the 2.1 MeV, 2.6 MeV, 3.4 MeV, and 4.2 MeV REPT electron fluxes on each

575 spacecraft. As we did for the proton pitch angle distributions, to help us identify intervals of
576 electron pitch angle scattering, we normalized the MagEIS and REPT electron fluxes in Figure 8
577 and Figure 9 to the values at 90° pitch angle. Thus, the flux at 90° degrees pitch angle is equal to
578 1, and the color bar indicates the fluxes at other pitch angles as a fraction of the flux at 90° degrees.
579 To reduce rapid time variations in the pitch angle distributions and make it easier to see large scale
580 features, we smoothed the pitch angle distributions with a running boxcar average of 7 spacecraft
581 spin periods. The light and dark grey boxes 1-8 and vertical lines mark the EMIC wave time
582 intervals.

583 On the outbound halves of the Van Allen Probes' orbits, some intermittent losses of
584 electrons appear at all of the energies shown in Figures 8 and 9. On RBSP-A during the outbound
585 half of orbit 3233, electron losses below about 70° and above 110° pitch angle occurred at 2.1
586 MeV, 2.6 MeV, and 3.4 MeV during EMIC wave bursts 2, 3 and 4. The losses appeared to be
587 most significant for burst 3 and portions of EMIC wave burst 4. Variations in the MagEIS 1.1
588 MeV and REPT 4.2 MeV electron pitch angle distributions are not clearly correlated with the
589 EMIC wave activity on RBSP-A during the outbound half of the orbit. On RBSP-B during the
590 outbound half of orbit 3214, electron losses above about 120° and below about 60° occurred at 2.1
591 MeV, 2.6 MeV, and 3.4 MeV occurred during EMIC wave bursts 2, 3, and 4. On RBSP-B, there
592 were electron losses at 4.2 MeV below 45° and above 130° pitch angle during EMIC wave bursts
593 2, 3, and 4. It was not clear if the variations in the RBSP-B MagEIS electron pitch angle
594 distributions at 1.1 MeV were due to the EMIC waves or just the general trend across the RBSP-
595 B orbit. Although the outbound EMIC wave bursts reached amplitudes up to 12 nT on RBSP-B,
596 these EMIC wave bursts had short time durations, which may explain why only patchy, light
597 electron scattering was observed during the outbound halves of the Van Allen Probes' orbits. In

addition, ULF waves in the Pc4-5 frequency bands with periods of 2-3 minutes were observed on the outbound halves of the orbits by both spacecraft, which may have resulted in competition between scattering processes due to the EMIC waves and acceleration and transport due to the ULF waves. On both spacecraft during the outbound halves of the orbits, it appears that the greatest losses of electrons at angles closest to 90° occurred at energies of 2.1 and 2.6 MeV during the EMIC wave bursts numbered 3 and 4.

On the inbound halves of the spacecraft orbits, the EMIC wave power was more sustained and more significant electron pitch angle scattering was observed. Figures 8 and 9 show that the electron pitch angle scattering on the inbound halves of the orbits varies with energy in a manner consistent with scattering by EMIC waves. On RBSP-A, on the inbound half of orbit 3233, there were electron losses in the MagEIS 1.1 MeV channel above 122° and below 57° pitch angle during EMIC wave burst 6, but the variations in the fluxes were not clearly correlated with the other wave bursts. Electron losses were also observed on RBSP-A for 2.1 MeV, 2.6 MeV, and 3.4 MeV above 110° and below 60° pitch angle throughout EMIC wave bursts 5-8, but the scattering reached angles closest to 90° during EMIC wave bursts 5 and 6. At 4.2 MeV, some electron losses were observed on RBSP-A above 120° and below 60° during bursts 5 and 6. On RBSP-B, on the inbound half of orbit 3214, the MagEIS 1.1 MeV channel showed some losses of electrons above 130° and below 60° pitch angle. At 2.1 MeV, there were significant losses above 100° and below 80° pitch angle, while at 3.4 MeV, there were losses above 110° and below 70°. At 4.2 MeV, there were electron losses above 120° and below 60° pitch angle. Comparison of the pitch angle distributions, before, during and after the inbound EMIC wave interval shows that pitch angle scattering losses of electrons at 2.1 and 2.6 MeV appears to be more significant than at the other energies shown. Although the time interval when EMIC waves were observed also corresponds

621 to the magnetospheric compression caused by the solar wind pressure increase, the energy and
622 pitch angle dependence of the electron flux decreases suggests that they were caused by the EMIC
623 waves and not by losses related to magnetopause shadowing. Magnetopause shadowing strongly
624 affects particles over a very broad range of energies. Scattering by EMIC waves affects mainly
625 particles at specific energies due to the nature of the resonant wave-particle interactions.
626
627 **9. Discussion**
628 **9.1 EMIC Wave Locations Relative to the Plasmapause and Local Time Extent**
629 The EMIC waves observed by the Van Allen Probes on 22 December 2015 associated with
630 increased solar wind dynamic pressure were found outside the plasmasphere, unlike the EMIC
631 waves associated with magnetospheric compressions observed by Usanova et al. [2010], which
632 were found in a high density region inside the plasmasphere. Tetrick et al. [2017] examined the
633 distance of the Van Allen Probes to the plasmapause when strong EMIC waves were observed
634 during the first local time rotation of the mission from 1 October 2012 to 13 July 2014. They
635 found most EMIC waves occurred within -1 to $+2R_E$ relative to the plasmapause. As indicated by
636 Table 1, during the outbound set of EMIC wave bursts on 22 December 2015, RBSP-A was located
637 between ΔL=+1.16 to +1.84 R_E outside the plasmasphere and RBSP-B was located between
638 ΔL=+0.84 to +1.53 R_E outside the plasmasphere. During the inbound set of EMIC wave bursts,
639 RBSP-A was located between ΔL=+2.02 to +1.42 R_E outside the plasmasphere and RBSP-B was
640 located between ΔL=+2.13 to +1.56 R_E outside the plasmasphere. Thus, the two intervals of EMIC
641 waves on 22 December 2015 we studied were observed mainly within +2 R_E of the plasmapause,
642 consistent with the results of Tetrick et al. [2017].
643 Blum et al. [2017] categorized Van Allen Probes EMIC wave observations from 2013-

644 2014 into three types of events: EMIC waves observed by one satellite, EMIC waves observed
645 simultaneously by both RBSP-A and RBSP-B, and EMIC waves observed by both satellites with
646 a time lag, similar to the separation time between the two spacecraft along their orbits. They
647 defined EMIC wave events as occurring simultaneously when the wave activity was observed by
648 both Van Allen Probes spacecraft with a time difference less than 5 minutes. During the outbound
649 half of the 22 December 2015 EMIC wave event, there was a 1 minute delay between the start of
650 the EMIC wave observations at RBSP-A and the start of the observations at RBSP-B, as shown
651 by Table 2. During the inbound half of this EMIC wave event, the delay between the start of
652 EMIC wave observations at RBSP-B and at RBSP-A was about 2 minutes and 15 seconds, as
653 shown by Table 3. Note that on the outbound half of its orbit, RBSP-A saw the EMIC waves first,
654 while on the inbound half of its orbit, RBSP-B saw them first, as shown by Figure 1 and Tables 2
655 and 3. As the time delay between the EMIC wave observations by both spacecraft was less than
656 5 minutes, the EMIC wave events studied in this paper would have fallen into the category of
657 simultaneous EMIC wave observations in the Blum et al. [2017] study.

658 Blum et al. [2017] found 70% of the EMIC wave events seen by both spacecraft had
659 separations of 0.5 R_E or less, while EMIC wave events with spacecraft separations greater than
660 ~1.5 R_E were mostly single spacecraft events. They also found that the average spacecraft
661 separation for the simultaneous EMIC wave events was 0.76 R_E, or 4842 km. The 22 December
662 2015 EMIC wave event studied here is consistent with the results from Blum et al. [2017]
663 regarding events observed simultaneously by both spacecraft, as the separations between the two
664 Van Allen Probes ranged from 0.56 to 0.68 R_E (3568-4332 km). The majority of the simultaneous
665 EMIC wave events found by Blum et al. [2017] also occurred beyond L=4, and had primarily
666 azimuthal rather than radial separations. The EMIC waves observed by the Van Allen Probes on

667 22 December 2015 occurred in a narrow L shell region from ~ 4.6-5.3 R_E between ~10-11 MLT
668 on the outbound halves of the spacecraft orbits. On the inbound halves of the spacecraft orbits,
669 the EMIC waves were found from L ~ 4.8-5.1 R_E between ~13-14 MLT. Thus, the range of L
670 shells where the EMIC waves were observed on 22 December 2015 is also consistent with the
671 results of Blum et al. [2017]. The L shell separations between RBSP-A and RBSP-B for the
672 outbound EMIC wave bursts ranged from 0.08 to 0.09 R_E (510-573 km) and for the inbound EMIC
673 wave bursts they ranges from 0.09 to 0.12 R_E (573-765 km). The MLT separations between RBSP-
674 A and RBSP-B for the outbound EMIC wave bursts were between 0.31 to 0.41 hours MLT and
675 for the inbound EMIC wave bursts they were between 0.44 to 0.50 hours MLT. At L=5, an
676 azimuthal separation of 0.5 hours MLT is equivalent to about 0.65 R_E, or 4141 km. Thus, as in
677 the Blum et al. [2017] study, the spacecraft had greater separations in the azimuthal direction than
678 in L shell during the EMIC wave bursts on 22 December 2015.

679 The regions of EMIC wave activity had a latitudinal extent of +0.22 degrees to -9.4 degrees
680 relative to the magnetic equator, based upon the locations of the EMIC wave observations by both
681 spacecraft shown in Tables 2 and 3. During the outbound EMIC wave bursts RBSP-A and RBSP-
682 B were also separated by 2.76° to 2.88° in magnetic latitude, and during the inbound wave bursts
683 they were separated by 3.12° to 3.15° in magnetic latitude. At L=5, a latitudinal separation of 3°
684 corresponds to about 0.26 R_E (1656 km).

685 As discussed earlier in this paper, the large spatial extent of the structure with increased
686 solar wind pressure inferred from Wind and ACE suggests that the entire dayside magnetosphere
687 should have been affected by the associated magnetospheric compressions. The similarities in the
688 spatial locations and structure of the EMIC observations by both spacecraft on the outbound and
689 inbound halves of the Van Allen Probes' orbits can be explained by a radially narrow region of

690 EMIC wave activity within ΔL=+1 to +2 R_E of the plasmapause across the dayside from 10 MLT
691 and 14 MLT on 22 December 2015 that persisted for at least 4.5 hours UT. Observations of the
692 type of extended region of EMIC wave activity we believe may have occurred on 22 December
693 2015 were reported on 23 February 2014 by Engebretson et al. [2015]. During the EMIC wave
694 event studied by Engebretson et al. [2015], increased solar wind dynamic pressure excited a region
695 of large amplitude H+ band waves that persisted for longer than 8 h in UT and covered more than
696 12 h in local time, from late morning through local noon, when the Van Allen Probes were outside
697 the plasmapause. The EMIC waves studied by Engebretson et al. [2015] were also observed by
698 ground-based magnetometers in Antarctica (near dawn), Finland (local noon), Russia (afternoon),
699 and Canada (from dusk to midnight). The occurrence of EMIC wave activity over an extended
700 dayside region of local time on 22 December 2015 would also be consistent with the study by
701 Blum et al. [2017] which showed that H+ band EMIC waves on the dayside often span large spatial
702 regions, as well as statistical studies of EMIC waves [Saikin et al., 2015] showing peak EMIC
703 wave occurrence rates across the day side.

704 The occurrence of an extended local time region of EMIC wave activity during the event
705 we studied in December 2015 would also be consistent with the Imager for Magnetopause-to-
706 Aurora Global Exploration (IMAGE) satellite data presented by Fuselier et al. [2004]. IMAGE
707 observed subauroral proton precipitation that Fuselier et al. [2004] believed to be caused by EMIC
708 waves across the entire dayside magnetosphere following a magnetospheric compression.
709 Subauroral 30-80 keV proton precipitation associated with magnetospheric compressions and
710 EMIC waves was also reported on 23 February 2014 by Engebretson et al. [2015] in NOAA Polar-
711 orbiting Operational Environmental Satellite (POES) and Meteorological Operational (MetOp)
712 satellite data near the northern foot point of the Van Allen Probes. Indeed, we found evidence for

713 proton scattering associated with the EMIC waves observed by the Van Allen Probes on 22
714 December 2015, which would be consistent with the results from Fuselier et al. [2004] and
715 Engebretson et al. [2015].

716 If there was a radially narrow region of EMIC wave activity outside the plasmapause across
717 the entire dayside magnetosphere on 22 December 2015, the Van Allen Probes briefly crossed
718 through one end of this narrow L shell region of EMIC wave activity on the outbound half of the
719 spacecraft orbits, and then crossed through the other end of this region of EMIC wave activity on
720 the inbound half of the spacecraft orbits. Although there are slight differences in the L shells where
721 the wave bursts occurred on the outbound and inbound halves of the orbits, this interpretation
722 would imply that the combinations of EMIC wave bursts 1 and 8, 2 and 7, 3 and 6, and 4 and 5 as
723 numbered in Figures 3-9 represent the pre-noon and afternoon halves of a longitudinally broad
724 region of EMIC wave activity and energetic particle precipitation extending across the day side
725 from 10 MLT to about 14 MLT. The differences in the start, peak, and end L shells of each EMIC
726 wave burst on the outbound and inbound halves of the orbit may be due to the differences in the
727 spacecraft latitudes on the outbound and inbound halves of these orbits, an asymmetry in the
728 structure of the magnetosphere in the morning and afternoon sector, or due to the temporal and
729 spatial evolution of the region of EMIC wave activity.

730 Although we do not have continuous satellite observations across the dayside to
731 conclusively prove this interpretation of the data, it appears highly likely that the EMIC waves did
732 occur across the entire dayside based upon the studies cited above and the observed wave burst
733 structures. Plasma in the dayside magnetosphere is often close to marginal stability for the ion
734 cyclotron instability, so even modest magnetospheric compressions can readily generate EMIC
735 waves [Anderson and Hamilton, 1993]. The generation of EMIC waves in narrow, marginally

736 unstable L shell regions outside the plasmapause after magnetospheric compressions could explain
737 some EMIC observations from the Time History of Events and Macroscale Interactions during
738 Substorms (THEMIS) and Polar satellites where the EMIC waves in space appeared to have short
739 time durations while Pc1-2 wave activity observed by ground magnetometer stations persisted for
740 hours [e.g. Engebretson et al., 2002; Usanova et al. 2008]. In some cases, the differences between
741 the duration of the EMIC waves in space and on the ground may be due to a combination of the
742 localization of the wave generation region in L shell, and the manner in which the spacecraft
743 traveled though this region.

744 THEMIS and Canadian Array for Realtime Investigations of Magnetic Activity
745 (CARISMA) observations have indicated that enhanced solar wind dynamic pressure is an
746 important source for radially confined EMIC emissions at lower-L shells close to the plasmapause,
747 because a compressed magnetosphere can enhance temperature anisotropy along the dayside ion
748 drift trajectories [Usanova et al., 2008]. The structure of the regions where the EMIC waves were
749 observed by the Van Allen Probes on 22 December 2015 may have been related to the ion drift
750 trajectories. On the afternoon side, during the inbound pass, the EMIC waves are more persistent
751 than the bursty waves that were observed on the morning side during the outbound pass. This is
752 possibly because ions injected at midnight will drift westward through dusk and encounter the
753 afternoon region first, before drifting around the dayside through noon and finally to the morning
754 side. It seems likely that the energy source driving the waves may have been more concentrated
755 on the afternoon side, closer to the source of the ions.

756

757 **9.2 Ion Composition and EMIC Waves**

Ion composition has been shown to affect the observed frequencies of EMIC waves as well as their occurrence during storms. Halford et al. [2010; 2016] found that CRRES observed EMIC waves most often during the storm main phase but noted that the EMIC wave occurrence rates dropped off to near 0 when Sym-H is less than – 75 nT. Based upon models showing that the relative oxygen concentration increases during the main phase [Glocer et al., 2009] and that increased levels of oxygen damp EMIC wave growth or limit the frequency range of EMIC waves [e.g., Omidi et al., 2013, Denton et al., 2014]. Halford et al. [2016] proposed that the presence of oxygen could explain the CRRES observations during the storm main phase. Halford et al. [2016] also noted that CRRES data indicated a rise in EMIC wave occurrence rates during the recovery phase. Data from the Van Allen Probes RBSPICE (Radiation Belt Storm Probes Ion Composition Experiment) have indicated that oxygen ions have a short lifetime in the ring current and that oxygen levels can fall off quickly during the recovery phases [Gerrard et al., 2014]. Halford et al. [2016] suggested that this behavior could explain the rise in EMIC wave occurrence during the recovery phase. However, as CRRES did not have the ion composition measurements required, Halford et al. [2016] could not directly test these hypotheses about the effects of oxygen ions on EMIC waves.

Although a detailed study of the effects of ion composition on EMIC waves during the 19-22 December 2015 storm is beyond the scope of this paper, we did consider the general trends shown in the HOPE ion composition data. The omnidirectional helium and oxygen fluxes measured by HOPE increased starting on 20 December 2015 shortly after the sudden commencement and remained at levels higher than their pre-storm values throughout the storm's main phase. The relative oxygen to proton density ratio was also elevated throughout the main phase, but began to decrease after the Dst minimum as the storm entered the recovery phase.

781 Although the helium fluxes increased during the main phase, the helium to oxygen density ratio
782 actually decreased during the main phase, and then began to increase late in the recovery phase.
783 On 22 December 2015, when the EMIC waves were observed during RBSP-A orbit 3233 and
784 RBSP-B orbit 3214, the oxygen densities were still higher than their pre-storm levels, but they
785 were slightly lower than they were during the main phase of this storm on 19-21 December 2015.
786 One interesting feature of the relative ion compositions during this event is that there were elevated
787 helium to oxygen density ratios during the outbound EMIC wave event on RBSP-A (check B).

788 During the outbound half of RBSP-A orbit 3233, when the EMIC waves were observed
789 the He/p+ ratio from HOPE was consistently between 0.1 and 0.2, while the He/O ratio took on
790 values over a slightly larger range between 0.1 to 0.3. During bursts 1 and 2, the O/p+ ratio was
791 steadily near 1, but it varied between 0.6-0.9 during bursts 3 and 4. During the inbound half of
792 RBSP-A orbit 3233 when the EMIC waves were observed, the He/p+ ratio varied between 0.1-
793 0.5, while the He/O ratio took on values between 0.2-0.5. The O/p+ ratio varied between about
794 0.6-0.9, consistent with the values seen on the outbound half of the orbit.

795 During the outbound half of RBSP-B orbit 3214, when the EMIC waves were observed the
796 He/p+ ratio from HOPE was consistently around 0.1, while the He/O ratio was more variable
797 between 0.07 to 0.2. The O/p+ ratio had values around 1.2 during bursts 1 and 2, but dropped to
798 values between 0.5-0.8 during bursts 3 and 4. Thus, the composition at RBSP-A and RBSP-B
799 appeared to have been similar during the outbound EMIC wave bursts. During the inbound half
800 of RBSP-B orbit 3214, the He/p+ ratio started out at about 0.1 during burst 5, and steadily increased
801 to about 0.2 by burst 8. The O/p+ ratio was consistently about 0.8 throughout the inbound set of
802 EMIC wave bursts, consistent with the observations at RBSP-A. The He/O ratio varied between
803 0.1-0.4. Overall, it appears that the levels of helium were slightly elevated during the inbound

804 halves of the orbits compared to the outbound halves at both RBSP-A and RBSP-B. The high
805 levels of helium are interesting as modeling of the effects of hot anisotropic He+ ions shows that
806 this should lead to the growth of EMIC waves in the He+ band and reduce EMIC wave growth
807 rates or lead to wave damping in the H+ band [Lee et al., 2017]. However, Lee et al. [2017] found
808 this effect was more pronounced in regions dominated by cold plasmas, such as inside the
809 plasmasphere or plumes, than it was for regions dominated by hot protons, such as outside the
810 plasmasphere.
811
812 **9.3 Pitch Angle Scattering and EMIC Wave Rising Tones**
813 The EMIC wave bursts examined in this paper included observations of rising tones, also
814 called triggered emissions, which are discrete wave structures similar to whistler mode chorus
815 elements that rapidly increase in frequency and rise up out of the main band of unstructured EMIC
816 waves [e.g., Pickett et al., 2010; Grison et al., 2016]. On both the outbound and inbound halves of
817 orbit 3233, RBSP-A observed several H+ band rising tones. Although the duration and timing of
818 the EMIC wave bursts observed by RBSP-B were nearly identical to those observed by RBSP-A,
819 RBSP-B did not see many rising tones during the outbound half of orbit 3214. However, on the
820 inbound half of orbit 3214, RBSP-B observed larger amplitude EMIC waves than RBSP-A and
821 more rising tones than RBSP-A. Some studies have suggested that EMIC waves with rising tones
822 are more effective at particle scattering than unstructured EMIC waves [Kubota and Omura, 2017;
823 Kubota et al., 2015]. A detailed analysis of the EMIC rising tone triggered emissions observed on
824 22 December 2015, including wave normal analysis, proton distribution functions, and the rising
825 tone frequency sweep rates will be covered in a separate paper.
826

9. Conclusions

The EMIC wave bursts we examined in this paper occurred during a close conjunction of the Van Allen Probes when Probe A and Probe B were separated by 0.57 to 0.68 R_E. Both Van Allen Probes spacecraft observed EMIC wave bursts within a 1-2 minute time delay with similar spatial structures. The EMIC waves were associated with enhanced solar wind dynamic pressure during the recovery phase of a CME driven geomagnetic storm and the spatial structure of the EMIC waves appeared to be correlated with total magnetic field strength variations produced by the solar wind pressure enhancements. Although the solar wind dynamic pressure enhancements had time durations of less than 1 hour, examination of Wind and ACE data indicated the dynamic pressure enhancements had a large spatial extent and were capable of impacting the entire dayside magnetosphere. The EMIC waves occurred outside the plasmasphere, within $\Delta L \sim 1\text{-}2\ R_E$ of the plasmapause and within a few degrees magnetic latitude of the equatorial plane. The EMIC waves were observed in a narrow L shell region from ~4.55-5.32 R_E between ~10-11 MLT on the outbound halves of the spacecraft orbits, and from L~4.82-5.51 R_E between ~13-14 MLT on the inbound halves of the spacecraft orbits. However, comparison with statistical studies of EMIC waves using Van Allen Probes data [Tetrick et al., Blum et al., Saikin et al.] as well as results from IMAGE on subauroral proton precipitation [Fuselier et al., 2004] suggests that there may have actually been a region of EMIC wave activity across the entire day side magnetosphere from 10 to 14 MLT. The anisotropy of the proton pitch angle distributions was enhanced above the Alfvén energy when EMIC waves were observed, possibly due to the effects of enhanced solar wind dynamic pressure and injections of fresh ions above about 10 keV. Although the overall radiation belt response during this storm was dominated by acceleration and transport processes, the EMIC waves produced local pitch angle scattering of 13-15 keV protons and 2.1-2.6 MeV electrons. The

strongest pitch angle scattering was observed on the inbound halves of the Van Allen Probes' orbits, when persistent EMIC wave activity with rising tones and amplitudes up to a few nT were observed.

Acknowledgments. This work was performed under JHU/APL contract no. 131802 under NASA prime contract no. NNN06AA01C. We acknowledge William Kurth for providing density calculations from the EMFISIS data. Processing and analysis of the HOPE, MagEIS, and REPT data was supported by the Energetic Particle, Composition, and Thermal Plasma (RBSP-ECT) investigation funded under NASA prime contract no. NAS5-01072. Data from the Van Allen Probes can be obtained through the Van Allen Probes Science Gateway (http://rbspgway.jhuapl.edu/). The Preliminary Reports and Forecasts of Solar Geophysical Data are available from the NOAA Space Weather Prediction Center (https://www.swpc.noaa.gov/). Solar wind data and geomagnetic indexes are available online from NASA OMNIWeb (https://omniweb.gsfc.nasa.gov/). Wind and ACE data are available online through CDAWeb (https://cdaweb.gsfc.nasa.gov/index.html/).

References

Allen, R. C., J.-C. Zhang, L. M. Kistler, H. E. Spence, R.-L. Lin, B. Klecker, M. W. Dunlop, M. André, and V. K. Jordanova (2015), A statistical study of EMIC waves observed by Cluster 1: Wave properties, *J. Geophys. Res.*, *120*, doi:10.1002/2015JA021333.

871 Anderson, B. J., and Hamilton, D. C. (1993), Electromagnetic ion cyclotron waves stimulated by
872 modest magnetospheric compressions, J. Geophys. Res., 98(A7), 11369–11382,
873 doi:10.1029/93JA00605.
874
875 Baker, D. N., S. G. Kanekal, V. C. Hoxie, S. Batiste, M. Bolton, X. Li, S. R. Elkington, S. Monk,
876 R. Reukauf, S. Steg, J. Westfall, C. Belting, B. Bolton, D. Braun, B. Cervelli, K. Hubbell M. Kien,
877 S. Knappmiller, S. Wade, B. Lamprecht, K. Stevens, J. Wallace, A. Yehle, H.E. Spence, R. Friedel
878 (2012), The Relativistic Electron-Proton Telescope (REPT) Instrument on Board the Radiation
879 Belt Storm Probes (RBSP) Spacecraft: Characterization of Earth's Radiation Belt High-Energy
880 Particle Populations, *Space Sci. Rev*., doi:10.1007/s11214-012-9950-9.
881
882 Balasis, G., Daglis, I. A., Contoyiannis, Y., Potirakis, S. M., Papadimitriou, C., Melis, N. S., et al.
883 (2018). Observation of intermittency-induced critical dynamics in geomagnetic field time series
884 prior to the intense magnetic storms of March, June, and December 2015. Journal of Geophysical
885 Research: Space Physics, 123, 4594–4613. https://doi.org/10.1002/2017JA025131
886
887 Blake, J. B., P. A. Carranza, S. G. Claudepierre, J. H. Clemmons, W. R. Crain Jr., Y. Dotan, J.F.
888 Fennell, F.H. Fuentes, R.M. Galvan, J.S. George, M.G. Henderson, M. Lalic, A.Y. Lin, M.D.
889 Looper, D.J. Mabry, J.E. Mazur, B. McCarthy, C.Q. Nguyen, T.P. O'Brien, M.A. Perez, M.T.
890 Redding, J.L. Roeder, D.J. Salvaggio, G.A. Sorensen, H.E. Spence, S. Yi, M. P. Zakrzewski
891 (2013), The Magnetic Electron Ion Spectrometer (MagEIS) Instruments Aboard the Radiation Belt
892 Storm Probes (RBSP) Spacecraft, *Space Sci. Rev.*, doi:10.1007/s11214-013-9991-8.
893

894 Blake, S. P., P. T. Gallagher, J. McCauley, A. G. Jones, C. Hogg, J. Campanya, C. Beggan, A. W.
895 P.Thomson, G. S. Kelly, and D. Bell (2016), Geomagnetically induced currents in the Irish power
896 network during geomagnetic storms, Space Weather, 14, 1136–1154,
897 doi:10.1002/2016SW001534.
898
899 Blum, L. W., J. W. Bonnell, O. Agapitov, K. Paulson, and C. Kletzing (2017), EMIC wave scale
900 size in the inner magnetosphere: Observations from the dual Van Allen Probes, Geophys. Res.
901 Lett., 44, 1227–1233, doi:10.1002/2016GL072316.
902
903 Bortnik, J., Omidi, N., Chen, L., Thorne, R. M., and Horne, R. B. (2011), Saturation characteristics
904 of electromagnetic ion cyclotron waves, J. Geophys. Res., 116, A09219,
905 doi:10.1029/2011JA016638.
906
907 Boyd, A. J., Turner, D. L., Reeves, G. D., Spence, H. E., Baker, D. N., & Blake, J. B. (2018). What
908 causes radiation belt enhancements: A survey of the Van Allen Probes Era. Geophysical Research
909 Letters, 45, 5253–5259. https://doi.org/10.1029/2018GL077699
910
911 Blagoveshchensky, Donat V., Olga A. Maltseva, and Maria A. Sergeeva (2018), Impact of
912 magnetic storms on the global TEC distribution, Ann. Geophys., 36, 1057–1071, 2018
913 https://doi.org/10.5194/angeo-36-1057-2018
914
915 Chashei, I. V., S. A. Tyul'bashev, V. I. Shishov, and I. A. Subaev (2016), Interplanetary and
916 ionosphere scintillation produced by ICME 20 December 2015, Space Weather, 14,

682–688, doi:10.1002/2016SW001455.

Cho, J.-H., D.-Y. Lee, S.-J. Noh, D.-K. Shin, J. Hwang, K.-C. Kim, J. J. Lee, C. R. Choi, S. Thaller, and R. Skoug (2016), Van Allen Probes observations of electromagnetic ion cyclotron waves triggered by enhanced solar wind dynamic pressure, J. Geophys. Res. Space Physics, 121, 9771–9793, doi:10.1002/2016JA022841.

Cornwall, J. M. (1965), Cyclotron instabilities and electromagnetic emission in the ultra low frequency and very low frequency ranges, J. Geophys. Res., 70(1), 61– 69, doi:10.1029/JZ070i001p00061.

Cornwall, J. M., and Schulz, M. (1971), Electromagnetic ion-cyclotron instabilities in multicomponent magnetospheric plasmas, J. Geophys. Res., 76(31), 7791–7796, doi:10.1029/JA076i031p07791.

Denton, R. E., V. K. Jordanova, and B. J. Fraser (2014), Effect of spatial density variation and O+ concentration on the growth and evolution of electromagnetic ion cyclotron waves, J. Geophys. Res. Space Physics, 119, 8372–8395, doi:10.1002/2014JA020384.

Elkington, S. R., M. K. Hudson, and A. A. Chan (1999), Acceleration of relativistic electrons via drift-resonant interaction with toroidal mode Pc5 oscillation, *Geophys. Res. Lett.*, *26*(21), 3273-3276.

940 Engebretson, M. J., W. K. Peterson, J. L. Posch, M. R. Klatt, B. J. Anderson, C. T. Russell, H. J.
941 Singer, R. L. Arnoldy, and H. Fukunishi (2002), Observations of two types of Pc 1 – 2 pulsations
942 in the outer dayside magnetosphere, J. Geophys. Res., 107(A12), 1451, doi:10.1029/
943 2001JA000198.
944
945 Engebretson, M. J., J. L. Posch, J. R. Wygant, C. A. Kletzing, M. R. Lessard, C.-L. Huang, H. E.
946 Spence, C. W. Smith, H. J. Singer, Y. Omura, R. B. Horne, G. D. Reeves, D. N. Baker, M.
947 Gkioulidou, K. Oksavik, I. R. Mann, T . Raita, and K. Shiokawa (2015), Van Allen probes, NOAA,
948 GOES, and ground observations of an intense EMIC wave event extending over 12 h in magnetic
949 local time, J. Geophys. Res. Space Physics, 120, 5465–5488, doi:10.1002/2015JA021227.
950
951 Fok, M.-C., G. V. Khazanov, E. N. Krivorutsky, and A. Glocer (2016), Convective growth of
952 electromagnetic ion cyclotron waves from realistic ring current ion distributions, J. Geophys. Res.
953 Space Physics, 121, 10,966–10,977, doi:10.1002/2016JA022964.
954
955 Funsten, H. O., R. M. Skoug, A. A. Guthrie, E. A. MacDonald, J. R. Baldonado, R. W. Harper,
956 K. C. Henderson, K. H. Kihara, J. E. Lake, B. A. Larsen, A. D. Puckett, V. J. Vigil, R. H. Friedel,
957 M. G. Henderson, J. T. Niehof, G. D. Reeves, M. F. Thomsen, J. J. Hanley, D. E. George, J.-M.
958 Jahn, S. Cortinas, A. De Los Santos, G. Dunn, E. Edlund, M. Ferris, M. Freeman, M. Maple, C.
959 Nunez, T. Taylor, W. Toczynski, C. Urdiales, H. E. Spence, J. A. Cravens, L. L. Suther, J. Chen
960 (2013). Helium, Oxygen, Proton, and Electron (HOPE) mass spectrometer for the Radiation Belt
961 Storm Probes mission. Space Science Reviews, 179, 423–484. https://doi.org/10.1007/s11214-
962 013-9968-7

963

964 Fuselier, S. A., S. P. Gary, M. F. Thomsen, E. S. Claflin, B. Hubert, B. R. Sandel, and T. Immel
965 (2004), Generation of transient dayside subauroral proton precipitation, J. Geophys. Res., 109,
966 A12227, doi:10.1029/2004JA010393.

967

968 Gao, Z., Z. Su, L. Chen, H. Zheng, Y. Wang and S. Wang (2017), Van Allen Probes observations
969 of whistler-mode chorus with long-lived oscillating tones, Geophys. Res. Lett., 44, 5909–5919,
970 doi:10.1002/2017GL073420.

971

972 Gerrard, A., L. Lanzerotti, M. Gkioulidou, D. Mitchell, J. Manweiler, J. Bortnik, and K. Keika
973 (2014), Initial measurements of O-ion and He-ion decay rates observed from the Van Allen probes
974 RBSPICE instrument, J. Geophys. Res. Space Physics, 119, 8813–8819,
975 doi:10.1002/2014JA020374.

976

977 Glocer, A., G. Tóth, T. Gombosi, and D. Welling(2009), Modeling ionospheric outflows and their
978 impact on the magnetosphere, initial results, J. Geophys. Res., 114, A05216,
979 doi:10.1029/2009JA014053.

980

981 Gomberoff, L., and Neira, R. (1983), Convective growth rate of ion cyclotron waves in a H+−He+
982 and H+−He+−O+ plasma, J. Geophys. Res., 88(A3), 2170– 2174, doi:10.1029/JA088iA03p02170.

983

984 Grison, B., F. Darrouzet, O. Santolík, N. Cornilleau-Wehrlin, and A. Masson (2016), Cluster
985 observations of reflected EMIC-triggered emission, Geophys. Res. Lett., 43, 4164–4171,

986 doi:10.1002/2016GL069096.
987
988 Halford, A. J., B. J. Fraser, S. K. Morley, S. R. Elkington, and A. A. Chan (2016), Dependence of
989 EMIC wave parameters during quiet, geomagnetic storm, and geomagnetic storm phase times, J.
990 Geophys. Res. Space Physics, 121, 6277–6291, doi:10.1002/2016JA022694.
991
992 Halford, A. J., B. J. Fraser, and S. K. Morley (2010), EMIC wave activity during geomagnetic
993 storm and nonstorm periods: CRRES results, J. Geophys. Res., 115, A12248,
994 doi:10.1029/2010JA015716.
995
996 Horne, R. B., R. M. Thorne, S. A. Glauert, N. P. Meredith, D. Pokhotelov, and O. Santolík (2007),
997 Electron acceleration in the Van Allen radiation belts by fast magnetosonic waves, *Geophys. Res.*
998 *Lett.*, *34*, L17107, doi:10.1029/2007GL030267.
999
1000 Horne, R. B., and R. M. Thorne (1998), Potential waves for relativistic electron scattering and
1001 stochastic acceleration during magnetic storms, *Geophys. Res. Lett.*, *25*(15), 3011-3014.
1002
1003 Horne, R. B., and Thorne, R. M. (1994), Convective instabilities of electromagnetic ion cyclotron
1004 waves in the outer magnetosphere, J. Geophys. Res., 99(A9), 17259–17273,
1005 doi:10.1029/94JA01259.
1006

1007 Jordanova, V. K., C. J. Farrugia, R. M. Thorne, G. V. Khazanov, G. D. Reeves, and M. F. Thomsen
1008 (2001), Modeling ring current proton precipitation by electromagnetic ion cyclotron waves during
1009 the May 14–16, 1997, storm, J. Geophys. Res., 106(A1), 7–22, doi:10.1029/2000JA002008.
1010
1011 Jordanova, V. K., J . U. Kozyra, and A . F. Nagy (1996b), Effects of heavy ions on the quasi-linear
1012 diffusion coefficients from resonant interactions with electromagnetic ion cyclotron waves, J.
1013 Geophys. Res., 101(A9), 19,771-19,778.
1014
1015 Jordanova, V. K., L. M. Kistler, J. U. Kozyra, G. V. Khazanov, and A. F. Nagy (1996a), Collisional
1016 losses of ring current ions, J. Geophys. Res., 101(A1), 111-126.
1017
1018 Kim, H.-J., and A. A. Chan (1997), Fully adiabatic changes in storm time relativistic electron
1019 fluxes, J. Geophys. Res., 102(A10), 22107–22116, doi:10.1029/97JA01814.
1020
1021 Kim, K. C., D.-Y. Lee, H.-J. Kim, L. R. Lyons, E. S. Lee, M. K. Öztürk, and C. R. Choi (2008),
1022 Numerical calculations of relativistic electron drift loss effect, *J. Geophys. Res.*, *113*, A09212,
1023 doi:10.1029/2007JA013011.
1024
1025 Kim, K.-H., Y. Omura, H. Jin, and J. Hwang (2017), A case study of EMIC waves associated with
1026 sudden geosynchronous magnetic field changes, J. Geophys. Res. Space Physics, 122,
1027 doi:10.1002/2016JA023391.
1028

1029 King, J. H. and N. E. Papitashvili (2005), Solar wind spatial scales in and comparisons of hourly
1030 Wind and ACE plasma and magnetic field data, *J. Geophys. Res.*, *110*, A02104,
1031 doi:10.1029/2004JA010649.
1032
1033 Kletzing, C. A., W.S. Kurth, M. Acuna, R. J. MacDowall, R. B. Torbert, T. Averkamp, D. Bodet,
1034 S. R. Bounds, M. Chutter, J. Connerney, D. Crawford, J. S. Dolan, R. Dvorsky, G. B. Hospodarsky,
1035 J. Howard, V. Jordanova, R. A. Johnson, D. L. Kirchner, B. Mokrzycki, G. Needell, J. Odom, D.
1036 Mark, R. Pfaff, J. R. Phillips, C. W. Piker, S. L. Remington, D. Rowland, O. Santolik, R. Schnurr,
1037 D. Sheppard, C. W. Smith, R. M. Thorne, J. Tyler (2013), The Electric and Magnetic Field
1038 Instrument Suite and Integrated Science (EMFISIS) on RBSP, *Space Sci. Rev.*, *179*, 127-181, doi:
1039 10.1007/s11214-013-9993-6.
1040
1041 Kozyra, J., T. Cravens, A. Nagy, E. Fontheim, and R. Ong (1984), Effects of Energetic Heavy Ions
1042 on Electromagnetic Ion Cyclotron Wave Generation in the Plasmapause Region, *J. Geophys. Res.*,
1043 *89*, 2217-2233.
1044
1045 Kubota, Y., and Y. Omura (2017), Rapid precipitation of radiation belt electrons induced by EMIC
1046 rising tone emissions localized in longitude inside and outside the plasmapause, J. Geophys. Res.
1047 Space Physics, 122, 293–309, doi:10.1002/2016JA023267.
1048
1049 Kubota, Y., Y. Omura, and D. Summers (2015), Relativistic electron precipitation induced by
1050 EMIC-triggered emissions in a dipole magnetosphere, J. Geophys. Res. Space Physics, 120, 4384–
1051 4399, doi:10.1002/2015JA021017.

Kurth, W. S., S. De Pascuale, J. B. Faden, C. A. Kletzing, G. B. Hospodarsky, S. Thaller, and J. R. Wygant (2015), Electron densities inferred from plasma wave spectra obtained by the Waves instrument on Van Allen Probes, *J. Geophys. Res.*, *120*, 904–914, doi:10.1002/2014JA020857.

Lee, D.-Y., S.-J. Noh, C.-R. Choi, J. J. Lee, and J. A. Hwang (2017), Effect of hot anisotropic He+ ions on the growth and damping of electromagnetic ion cyclotron waves in the inner magnetosphere, J. Geophys. Res. Space Physics, 122, 4935–4942, doi:10.1002/2016JA023826.

Li, X., D. N. Baker, M. Temerin, T. E. Cayton, E. G. D. Reeves, R. A. Christensen, J. B. Blake, M. D. Looper, R. Nakamura, and S. G. Kanekal (1997), Multisatellite observations of the outer zone electron variation during the November 3–4, 1993, magnetic storm, *J. Geophys. Res.*, *102*(A7), 14123–14140, doi:10.1029/97JA01101.

Liu, Yi A., Ying D. Liu, Huidong Hu, Rui Wang, and Xiaowei Zhao (2018). Multi-spacecraft Observations of the Rotation and Nonradial Motion of a CME Flux Rope Causing an Intense Geomagnetic Storm, The Astrophysical Journal, 854:126 (8pp), https://doi.org/10.3847/1538-4357/aaa959

Loto'aniu, T. M., B. J. Fraser, and C. L. Waters (2005), Propagation of electromagnetic ion cyclotron wave energy in the magnetosphere, J. Geophys. Res., 110, A07214, doi:10.1029/2004JA010816.

1075 Loucks, D., S. Palo, M. Pilinski, G. Crowley, I. Azeem, and D. Hampton (2017), High-latitude
1076 GPS phase scintillation from E region electron density gradients during the 20–21 December 2015
1077 geomagnetic storm, J. Geophys. Res. Space Physics, 122, 7473–7490,
1078 doi:10.1002/2016JA023839.
1079
1080 Mace, R. L., R. D. Sydora, and I. Silin (2011), Effects of superthermal ring current ion tails on the
1081 electromagnetic ion cyclotron instability in multi-ion magnetospheric plasmas, J. Geophys. Res.,
1082 116, A05206, doi:10.1029/2010JA016393.
1083
1084 Mansilla, Gustavo A (2019). Behavior of the Total Electron Content over the Arctic and Antarctic
1085 sectors during several intense geomagnetic storms, Geodesy and Geodynamics 10, 26-36,
1086 https://doi.org/10.1016/j.geog.2019.01.004
1087
1088 McCollough, J. P., S. R. Elkington, M. E. Usanova, I. R. Mann, D. N. Baker, and Z. C. Kale
1089 (2010), Physical mechanisms of compressional EMIC wave growth, J. Geophys. Res., 115,
1090 A10214, doi:10.1029/2010JA015393.
1091
1092 McCollough, J. P., S. R. Elkington, and D. N. Baker (2012), The role of Shabansky orbits in
1093 compression-related electromagnetic ion cyclotron wave growth, J. Geophys. Res., 117, A01208,
1094 doi:10.1029/2011JA016948.
1095

1096 Meredith, N. P., R. M. Thorne, R. B. Horne, D. Summers, B. J. Fraser, and R. R. Anderson (2003),
1097 Statistical analysis of relativistic electron energies for cyclotron resonance with EMIC waves
1098 observed on CRRES, *J. Geophys. Res.*, *108*(A6), 1250, doi:10.1029/2002JA009700.
1099
1100 Min, K., J. Lee, K. Keika, and W. Li (2012), Global distribution of EMIC waves derived from
1101 THEMIS observations, *J. Geophys. Res.*, *117*, A05219, doi:10.1029/2012JA017515.
1102
1103 Min, K., and K. Liu (2016), Proton velocity ring-driven instabilities in the inner magnetosphere:
1104 Linear theory and particle-in-cell simulations, J. Geophys. Res. Space Physics, 121, 475–491,
1105 doi:10.1002/2015JA022042.
1106
1107 Mithaiwala, M., C. Crabtree, G. Ganguli, L. Rudakov, and K. Keika (2013), Convective
1108 amplification of electromagnetic ion cyclotron waves from ring-distribution protons in the inner
1109 magnetosphere, J. Geophys. Res. Space Physics, 118, 7538–7544, doi:10.1002/2013JA019134.
1110
1111 Olson, W. P., and Pfitzer, K. A. (1982), A dynamic model of the magnetospheric magnetic and
1112 electric fields for July 29, 1977, J. Geophys. Res., 87(A8), 5943–5948,
1113 doi:10.1029/JA087iA08p05943.
1114
1115 Pickett, J. S., et al. (2010), Cluster observations of EMIC triggered emissions in association with
1116 Pc1 waves near Earth's plasmapause, Geophys. Res. Lett., 37, L09104,
1117 doi:10.1029/2010GL042648.
1118

1119 Saikin, A. A., J.-C. Zhang, R. C. Allen, C. W. Smith, L. M. Kistler, H. E. Spence, R. B. Torbert,
1120 C. A. Kletzing, and V. K. Jordanova (2015), The occurrence and wave properties of H+-, He+-,
1121 and O+-band EMIC waves observed by the Van Allen Probes, J. Geophys. Res. Space Physics,
1122 120, 7477–7492, doi:10.1002/2015JA021358.
1123
1124 Shabansky, V. P. (1971), Some processes in the magnetosphere, Space Sci. Rev., 12(3), 299.
1125
1126 Spence, H. E., et al. (2013), Science goals and overview of the Radiation Belt Storm Probes
1127 (RBSP) Energetic Particle, Composition, and Thermal Plasma (ECT) suite on NASA's Van
1128 Allen Probes mission, Space Sci. Rev., 179, 311–336, doi:10.1007/978-1-4899-7433-4_10.
1129
1130 Summers, D., R. M. Thorne, and F. L. Xiao (1998), Relativistic theory of wave-particle resonant
1131 diffusion with application to electron acceleration in the magnetosphere, J. Geophys. Res., 103,
1132 20,487.
1133
1134 Takahashi, K. and A. Y. Ukhorskiy (2007), Solar wind control of Pc5 pulsation power at
1135 geosynchronous orbit, *J. Geophys. Res.*, *112*, A11205, doi:10.1029/2007JA012483.
1136
1137 Tetrick, S. S., M. J. Engebretson, J. L. Posch, C. N. Olson, C.W. Smith, R. E. Denton, S. A. Thaller,
1138 J. R. Wygant, G. D. Reeves, E. A. MacDonald, and J. F. Fennell (2017), Location of intense
1139 electromagnetic ion cyclotron (EMIC) wave events relative to the plasmapause: Van Allen Probes
1140 observations, J. Geophys. Res. Space Physics, 122, doi:10.1002/2016JA023392.
1141

1142 Thorne, R. M., W. Li, B. Ni, Q. Ma, J. Bortnik, L. Chen, D. N. Baker, H. E. Spence, G. D. Reeves,
1143 M. G. Henderson, C. A. Kletzing, W. S. Kurth, G. B. Hospodarsky, J. B. Blake, J. F. Fennell, S.
1144 G. Claudepierre, and S. G. Kanekal (2013a), Rapid local acceleration of relativistic radiation-belt
1145 electrons by magnetospheric chorus, *Nature*, *504*, 411–414, doi:10.1038/nature12889.
1146
1147 Ukhorskiy A. Y., Y. Y. Shprits, B. J. Anderson, K. Takahashi, R. M. Thorne, (2010), Rapid
1148 scattering of radiation belt electrons by storm-time EMIC waves, Geophysical Research Letters,
1149 37, doi:10.1029/2010GL042906
1150
1151 Usanova, M. E., I. R. Mann, I. J. Rae, Z. C. Kale, V. Angelopoulos, J. W. Bonnell, K.-H.
1152 Glassmeier, H. U. Auster, and H. J. Singer (2008), Multipoint observations of magnetospheric
1153 compression-related EMIC Pc1 waves by THEMIS and CARISMA, Geophys. Res. Lett., 35,
1154 L17S25, doi:10.1029/2008GL034458.
1155
1156 Usanova, M. E., et al. (2010), Conjugate ground and multisatellite observations of compression-
1157 related EMIC Pc1 waves and associated proton precipitation, J. Geophys. Res., 115, A07208,
1158 doi:10.1029/2009JA014935.
1159
1160 Usanova, M. E., et al. (2014), Effect of EMIC waves on relativistic and ultrarelativistic electron
1161 populations: Groundbased and Van Allen Probes observations, Geophys. Res. Lett., 41, 1375–
1162 1381, doi:10.1002/2013GL059024.
1163

1164 Usanova, M. E., and Ian R. Mann (2016), Understanding the Role of EMIC Waves in Radiation
1165 Belt and Ring Current Dynamics: Recent Advances, in *Waves, Particles, and Storms in Geospace:*
1166 *A Complex Interplay*, edited by Georgios Balasis, Ioannis A. Daglis, and Ian R. Mann, Oxford
1167 University Press, DOI:10.1093/acprof:oso/9780198705246.003.0011.
1168
1169 Wang, J., Morton, Y. J., & Hampton, D. (2018). New results on ionospheric irregularity drift
1170 velocity estimation using multi-GNSS spaced-receiver array during high-latitude phase
1171 scintillation. Radio Science, 53, 228–240. https://doi.org/10.1002/2017RS006470
1172
1173 West, H. I., R. M. Buck, and J. R. Walton (1972), Shadowing of Electron Azimuthal-Drift Motions
1174 near the Noon Magnetopause, Nature Physical Science, 240, 6-7.
1175
1176 Yu, X., Yuan, Z., Huang, S., Yao, F., Wang, D., Funsten, H. O., & Wygant, J. R. (2018). Excitation
1177 of O+ band EMIC waves through H+ ring velocity distributions: Van Allen Probe observations.
1178 Geophysical Research Letters, 45, 1271–1276. https://doi.org/10.1002/2018GL077109.
1179
1180 Zhang, D., Liu, W., Li, X., Sarris, T., Xiao, C., & Wygant, J. R. (2018). Observations of impulsive
1181 electric fields induced by interplanetary shock. Geophysical Research Letters, 45, 7287–7296.
1182 https://doi.org/10.1029/2018GL078809
1183
1184 Zakharenkova, I., & Cherniak, I. (2018). Underutilized spaceborne GPS observations for space
1185 weather monitoring. Space Weather, 16, 345–362. https://doi.org/10.1002/2017SW001756
1186

Figure Captions

Figure 1. An overview of the 19- 22 December 2015 geomagnetic storm showing the OMNI solar wind flow speed, dynamic pressure, and interplanetary magnetic field (IMF) Bz GSM, Van Allen Probe A (RBSP-A) REPT 2.6 MeV electrons as a function of L shell and time, the Dst index, and the Kp index. OMNI solar wind parameters have been propagated to the Earth's bow shock. The vertical lines mark times on 22 December 2015 when the Van Allen Probes observed EMIC waves associated with magnetospheric compressions during the recovery phase of this storm.

Figure 2. Orbits 3233 (RBSP-A) and 3214 (RBSP-B) of the Van Allen Probes on 22 December 2015. The top panel shows the orbits of RBSP-A (red) and RBSP-B (blue) as a function of L shell and MLT. The second panel shows the orbits of RBSP-A and RBSP-B viewed through the noon meridian as a function of L shell and magnetic latitude. The intervals of EMIC waves are marked with heavy lines, and the start of each interval is marked with a *. The locations of each plasmapause crossing has been marked with a green X.

Figure 3. The top and bottom panels show FFT spectrograms of the EMFISIS fluxgate magnetometer B_Y components of the magnetic field in solar magnetic (SM) coordinates and a line plot of the total magnetic field from RBSP-A orbit 3233 and RBSP-B orbit 3214. The center panel shows the OMNI 1 minute solar wind dynamic pressure shifted to the Earth's bow shock. The H+ and He+ ion gyrofrequencies have been overplotted with white lines on the spectrograms, and the times of the outbound and inbound EMIC wave intervals have been marked with vertical magenta

1209 lines. The alternating light and dark grey boxes numbered 1-8 mark the individual EMIC wave
1210 bursts.
1211
1212 **Figure 4.** Overview of Van Allen Probe A EMFISIS magnetic field and HOPE proton data. The
1213 top panel shows an FFT spectrogram of the B_Y SM component of the magnetic field with the H+
1214 and He+ ion gyrofrequencies overplotted in white. The second panel shows the temperature
1215 anisotropy $T_\perp/T_\parallel$ from the HOPE proton moments. The third panel shows the proton pitch angle
1216 distribution anisotropy (difference between the parallel and perpendicular fluxes divided by the
1217 total flux) from HOPE for energies between 1 and 50 keV, with the energy E_A of a proton at the
1218 Alfvén speed overplotted in black. The proton anisotropy is only plotted when the total proton
1219 flux at each energy is greater than 65,000 $s^{-1}cm^{-2}ster^{-1}keV^{-1}$. The bottom two panels show the
1220 parallel (mean of 4.5°, 18.0°, and 36.0° pitch angles) and perpendicular (90° pitch angle) HOPE
1221 proton fluxes, with E_A overplotted in white. The alternating light and dark grey boxes 1-8 and
1222 vertical magenta lines mark the EMIC waves.
1223
1224 **Figure 5.** Overview of Van Allen Probe B magnetic field and HOPE proton data in the same
1225 format as Figure 5.
1226
1227 **Figure 6.** An FFT spectrogram of the B_Y SM magnetic field and HOPE pitch angle distributions
1228 as a function of time from RBSP-A orbit 3233 for protons with energies of 9.6 keV, 13.1 keV,
1229 15.2 keV, and 20.7 keV. We normalized the HOPE proton fluxes to the value at 90° pitch angle,
1230 to make it easier to identify proton scattering. Thus, the flux at 90° pitch angle in Figure 6 is equal
1231 to 1, and the color bar indicates the fluxes at other pitch angles as a fraction of the flux at 90°. To

reduce noise in the pitch angle distributions, we smoothed them with a running boxcar average of 7 spacecraft spin periods. The alternating light and dark grey boxes 1-8 and vertical magenta lines mark the EMIC waves.

Figure 7. An FFT spectrogram of the B_Y SM magnetic field and HOPE pitch angle distributions as a function of time from RBSP-B orbit 3214 for protons with energies of 9.6 keV, 13.1 keV, 15.2 keV, and 20.7 keV in the same format as Figure 6.

Figure 8. An FFT spectrogram of the B_Y SM magnetic field from RBSP-A orbit 3233 and pitch angle distributions of the MagEIS 1.1 MeV electron fluxes and pitch angle distributions of the 2.1, 2.6, 3.4, and 4.2, MeV REPT electron fluxes. We normalized the MagEIS and REPT electron fluxes in Figure 8 to the values at 90° pitch angle. Thus, the flux at 90° pitch angle in Figure 6 is equal to 1, and the color bar indicates the fluxes at other pitch angles as a fraction of the flux at 90°. To reduce noise in the electron pitch angle distributions, we smoothed them with a running boxcar average of 7 spacecraft spin periods. The alternating light and dark grey boxes 1-8 and vertical magenta lines mark the EMIC waves.

Figure 9. An FFT spectrogram of the B_Y SM magnetic field from RBSP-B orbit 3214 and MagEIS and REPT electron pitch angle distributions in the same format as Figure 8.

Table 1.

EMFISIS Upper Hybrid Line Plasmapause Crossings RBSP-A Orbit 3233 and RBSP-B Orbit 3214					
	Time UT	SM (X ,Y,Z) (R_E)	L Shell (R_E)	MLT (hours)	MLAT (degrees)
Outbound					
RBSP-A	2015-12-22T05:35:49	(2.50,-2.42,0.06)	3.48	9.06	0.91
RBSP-B	2015-12-22T05:50:08	(2.60,-2.62,0.16)	3.71	8.99	2.51
Inbound					
RBSP-A	2015-12-22T12:06:56	(1.93,2.47,-0.75)	3.40	15.46	-13.4
RBSP-B	2015-12-22T12:17:49	(2.19,2.32,-0.62)	3.38	15.11	-11.05

Table 2.

Outbound EMIC Wave Burst Locations and Spacecraft Separations						
	Start	L Shell (R_E)	MLT (Hours)	MLAT (Degrees)	SM (X,Y,Z) (R_E)	Spacecraft Separation (R_E)
RBSP-A						
Start	2015-12-22T 06:28:33	4.65	10.32	-2.59	(4.2,-1.97,-0.21)	0.57
End	2015-12-22T07:14:33	5.32	11.06	-4.25	(5.12,-1.28,-0.39)	0.61
RBSP-B						
Start	2015-12-22T06:28:54	4.55	10.00	0.22	(3.88,-2.38,0.02)	0.57
End	2015-12-22T07:15:15	5.25	10.66	-1.39	(4.92,-1.80,-0.13)	0.61

Table 3.

Inbound EMIC Wave Burst Locations and Spacecraft Separations						
	Start	L Shell (R_E)	MLT (Hours)	MLAT (Degrees)	SM (X,Y,Z) (R_E)	Spacecraft Separation (R_E)
RBSP-A						
Start	2015-12-22T10:16:14	5.42	13.26	-8.0	(4.98,1.71,-0.74)	0.68
End	2015-12-22T11:01:36	4.82	13.93	-9.40	(4.05,2.24,-0.76)	0.68
RBSP-B						
Start	2015-12-22T10:14:58	5.51	12.82	-4.87	(5.33,1.16,-0.46)	0.68
End	2015-12-22T11:02:16	4.96	13.45	-6.22	(4.52,1.80,-0.53)	0.68

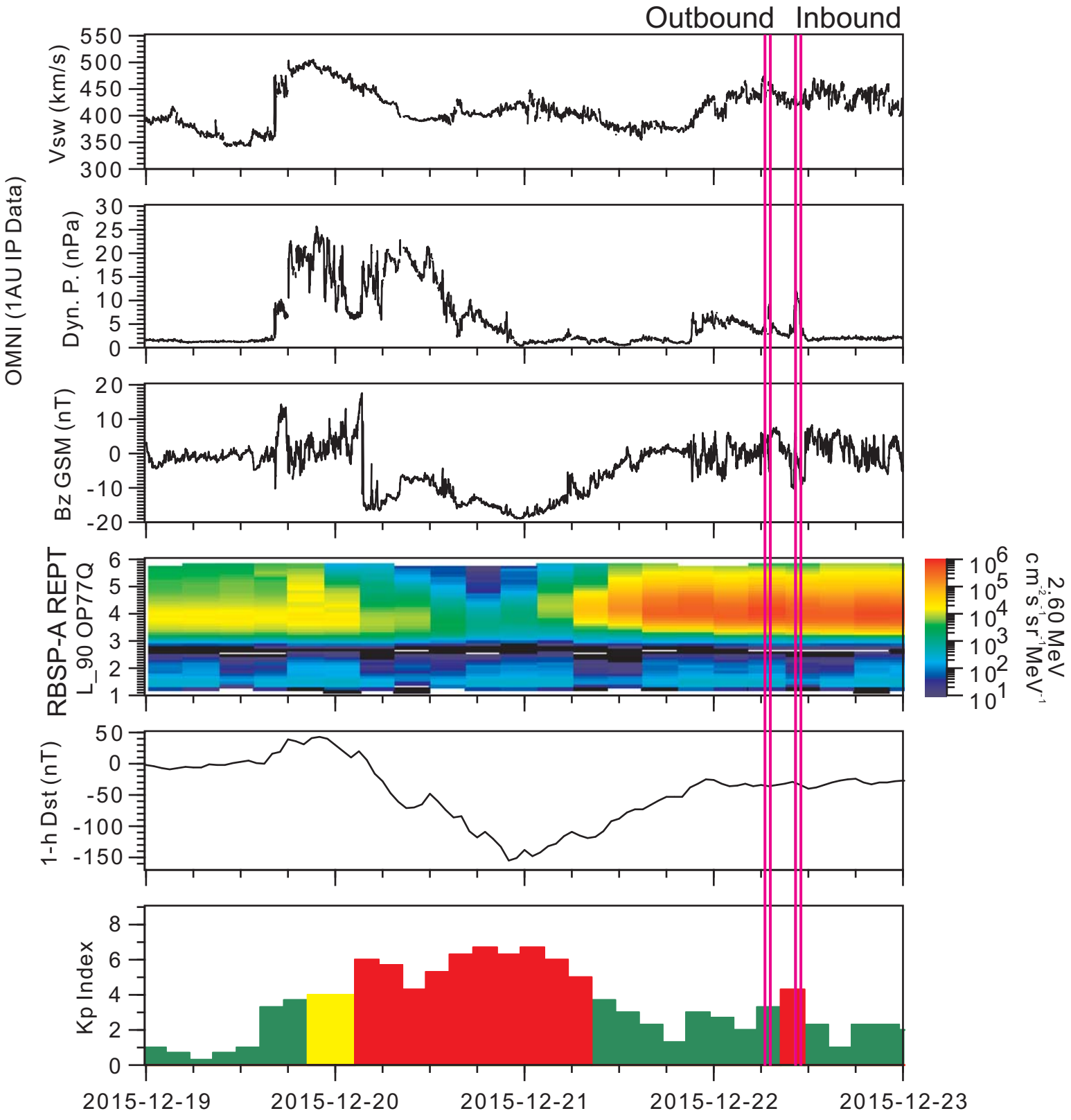
Outbound
Inbound
OMNI (1AU IP Data)
Vsw (km/s)
550
500
450
400
350
300
Dyn. P. (nPa)
30
25
20
15
10
5
0
Bz GSM (nT)
20
10
0
-10
-20
RBSP-A REPT
L_90 OP77Q
6
5
4
3
2
1
2.60 MeV
cm-2 s-1 sr-1 MeV-1
10^6
10^5
10^4
10^3
10^2
10^1
1-h Dst (nT)
50
0
-50
-100
-150
Kp Index
8
6
4
2
0
2015-12-19
2015-12-20
2015-12-21
2015-12-22
2015-12-23

Figure 1

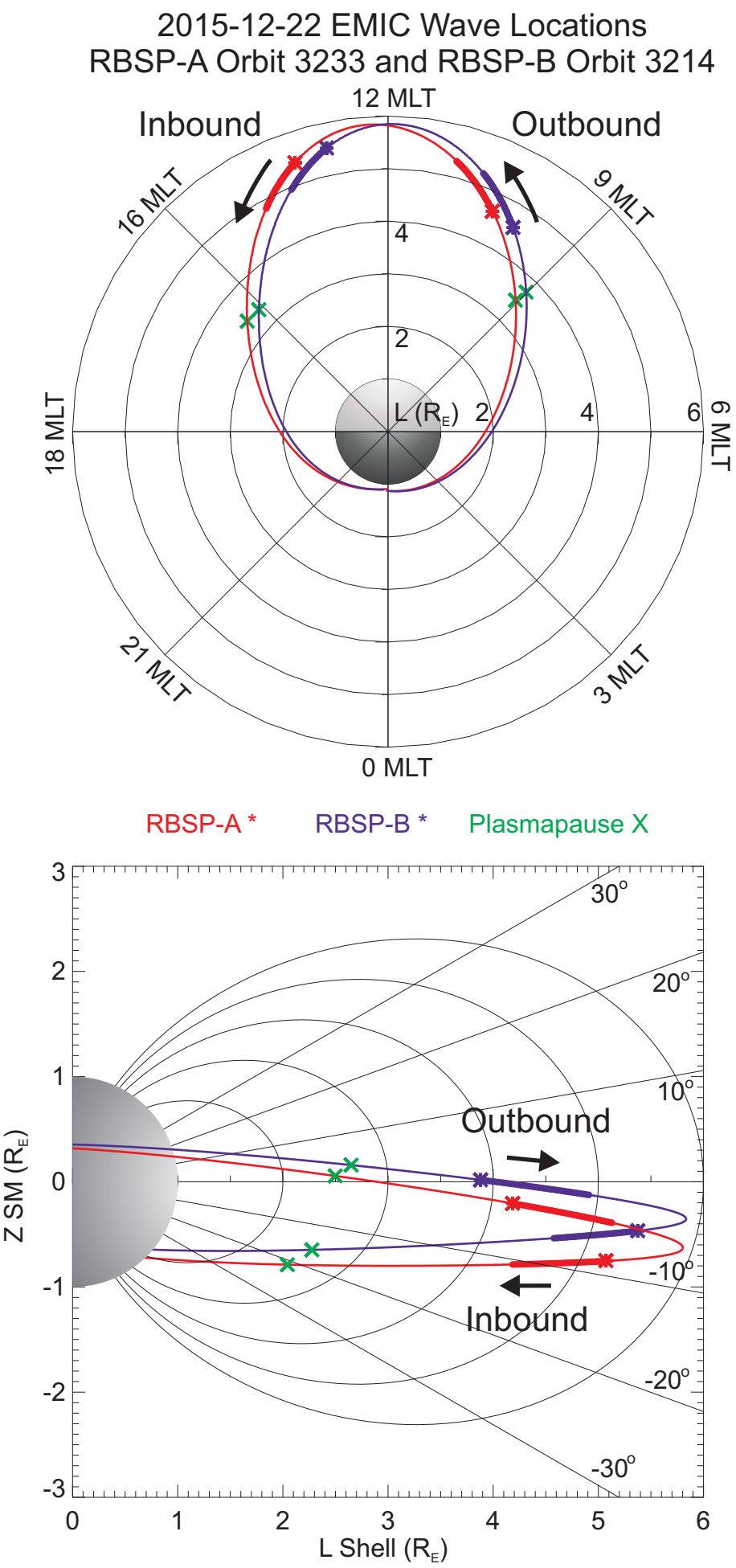
2015-12-22 EMIC Wave Locations
RBSP-A Orbit 3233 and RBSP-B Orbit 3214
12 MLT
Inbound
Outbound
16 MLT
9 MLT
4
2
L (R_E) 2
4
6
18 MLT
6 MLT
21 MLT
3 MLT
0 MLT
RBSP-A *
RBSP-B *
Plasmapause X
30°
20°
10°
Outbound
-10°
Inbound
-20°
-30°
Z SM (R_E)
L Shell (R_E)

Figure 2

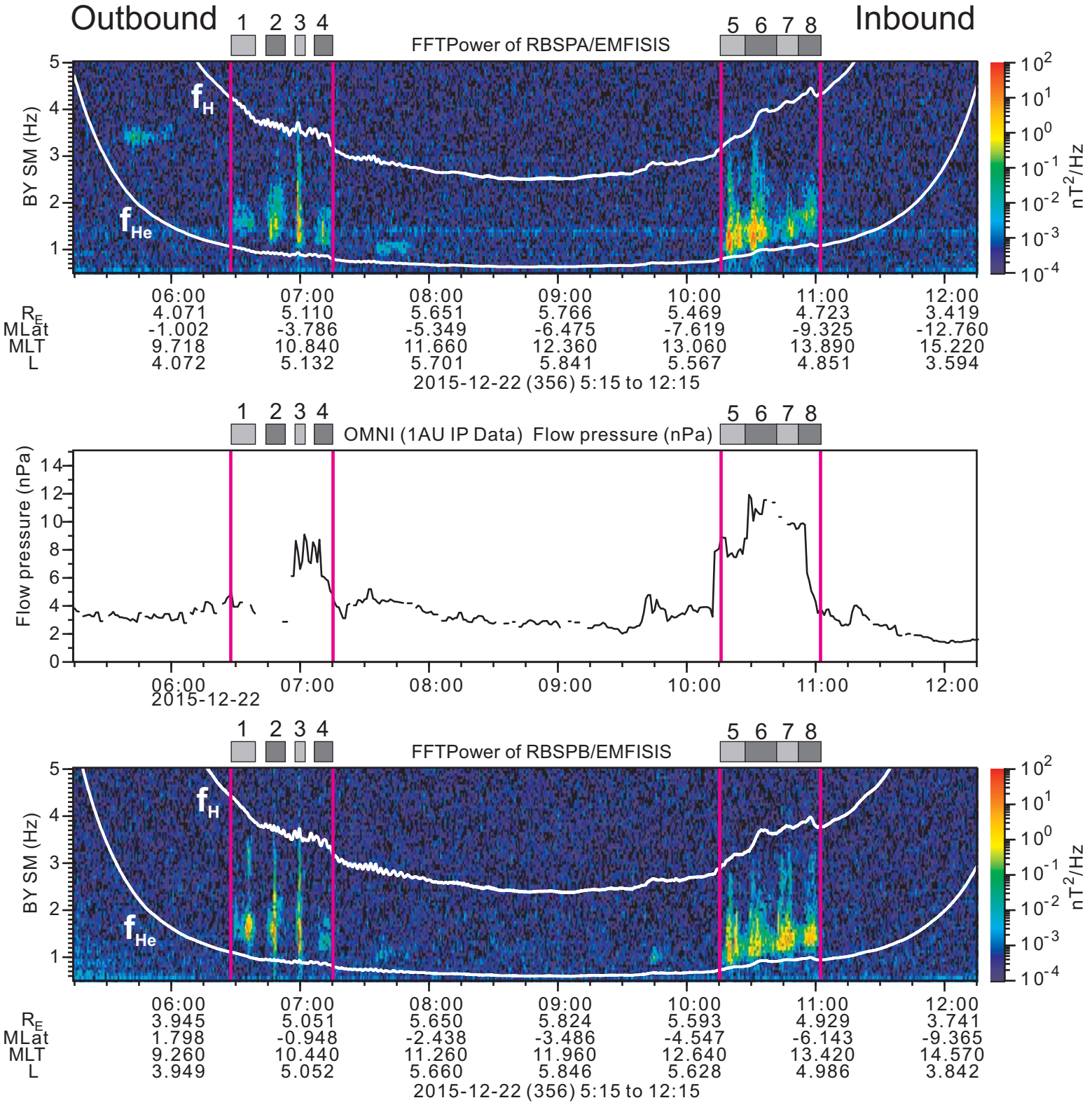
Outbound
Inbound
1 2 3 4
5 6 7 8
FFTPower of RBSPA/EMFISIS
BY SM (Hz)
f_H
f_{He}
nT²/Hz
06:00 07:00 08:00 09:00 10:00 11:00 12:00
R_E 4.071 5.110 5.651 5.766 5.469 4.723 3.419
MLat -1.002 -3.786 -5.349 -6.475 -7.619 -9.325 -12.760
MLT 9.718 10.840 11.660 12.360 13.060 13.890 15.220
L 4.072 5.132 5.701 5.841 5.567 4.851 3.594
2015-12-22 (356) 5:15 to 12:15
OMNI (1AU IP Data) Flow pressure (nPa)
Flow pressure (nPa)
2015-12-22
FFTPower of RBSPB/EMFISIS
R_E 3.945 5.051 5.650 5.824 5.593 4.929 3.741
MLat 1.798 -0.948 -2.438 -3.486 -4.547 -6.143 -9.365
MLT 9.260 10.440 11.260 11.960 12.640 13.420 14.570
L 3.949 5.052 5.660 5.846 5.628 4.986 3.842
2015-12-22 (356) 5:15 to 12:15

Figure 3

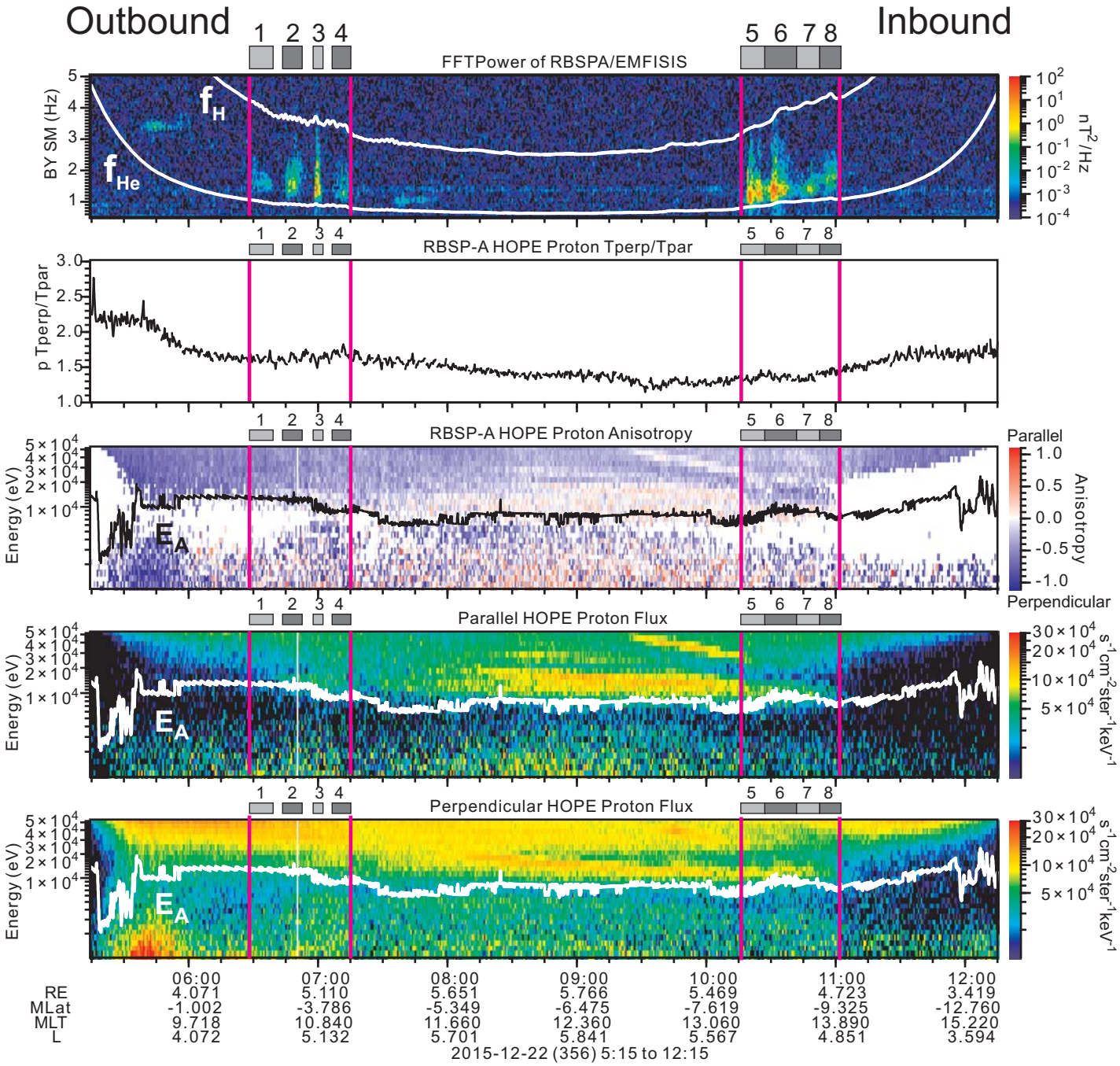
Outbound
Inbound
1 2 3 4
5 6 7 8
FFTPower of RBSPA/EMFISIS
BY SM (Hz)
f_H
f_{He}
nT^2/Hz
RBSP-A HOPE Proton Tperp/Tpar
p Tperp/Tpar
RBSP-A HOPE Proton Anisotropy
Energy (eV)
E_A
Parallel
Perpendicular
Anisotropy
Parallel HOPE Proton Flux
Perpendicular HOPE Proton Flux
$s^{-1}cm^{-2}ster^{-1}keV^{-1}$
RE 4.071 5.110 5.651 5.766 5.469 4.723 3.419
MLat -1.002 -3.786 -5.349 -6.475 -7.619 -9.325 -12.760
MLT 9.718 10.840 11.660 12.360 13.060 13.890 15.220
L 4.072 5.132 5.701 5.841 5.567 4.851 3.594
06:00 07:00 08:00 09:00 10:00 11:00 12:00
2015-12-22 (356) 5:15 to 12:15

Figure 4

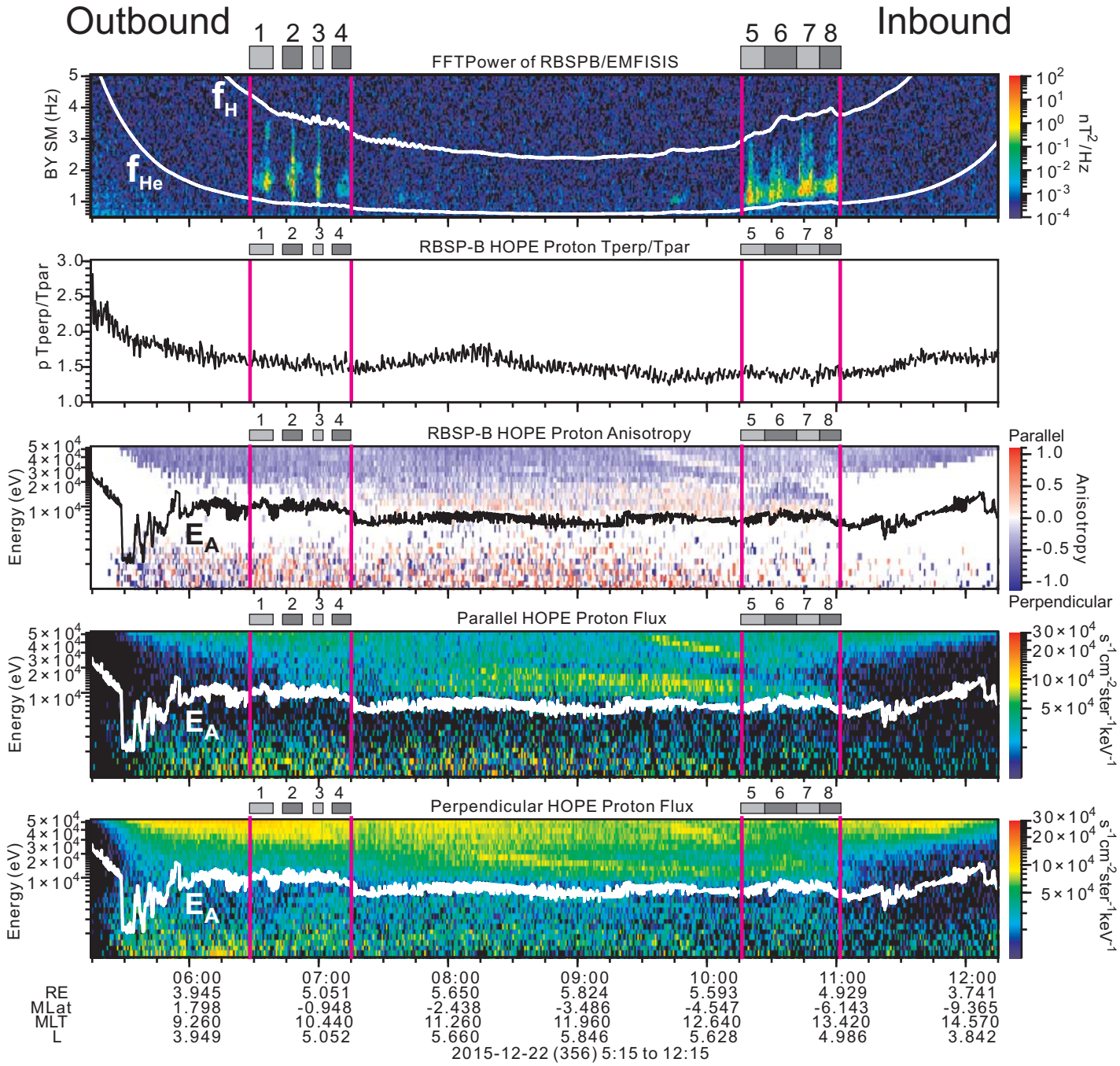
Outbound
Inbound
1 2 3 4
5 6 7 8
FFTPower of RBSPB/EMFISIS
BY SM (Hz)
f_H
f_{He}
nT^2/Hz
RBSP-B HOPE Proton Tperp/Tpar
p Tperp/Tpar
RBSP-B HOPE Proton Anisotropy
Energy (eV)
E_A
Parallel
Anisotropy
Perpendicular
Parallel HOPE Proton Flux
Perpendicular HOPE Proton Flux
$s^{-1}cm^{-2}ster^{-1}keV^{-1}$
RE
MLat
MLT
L
06:00 07:00 08:00 09:00 10:00 11:00 12:00
3.945 5.051 5.650 5.824 5.593 4.929 3.741
1.798 -0.948 -2.438 -3.486 -4.547 -6.143 -9.365
9.260 10.440 11.260 11.960 12.640 13.420 14.570
3.949 5.052 5.660 5.846 5.628 4.986 3.842
2015-12-22 (356) 5:15 to 12:15

Figure 5

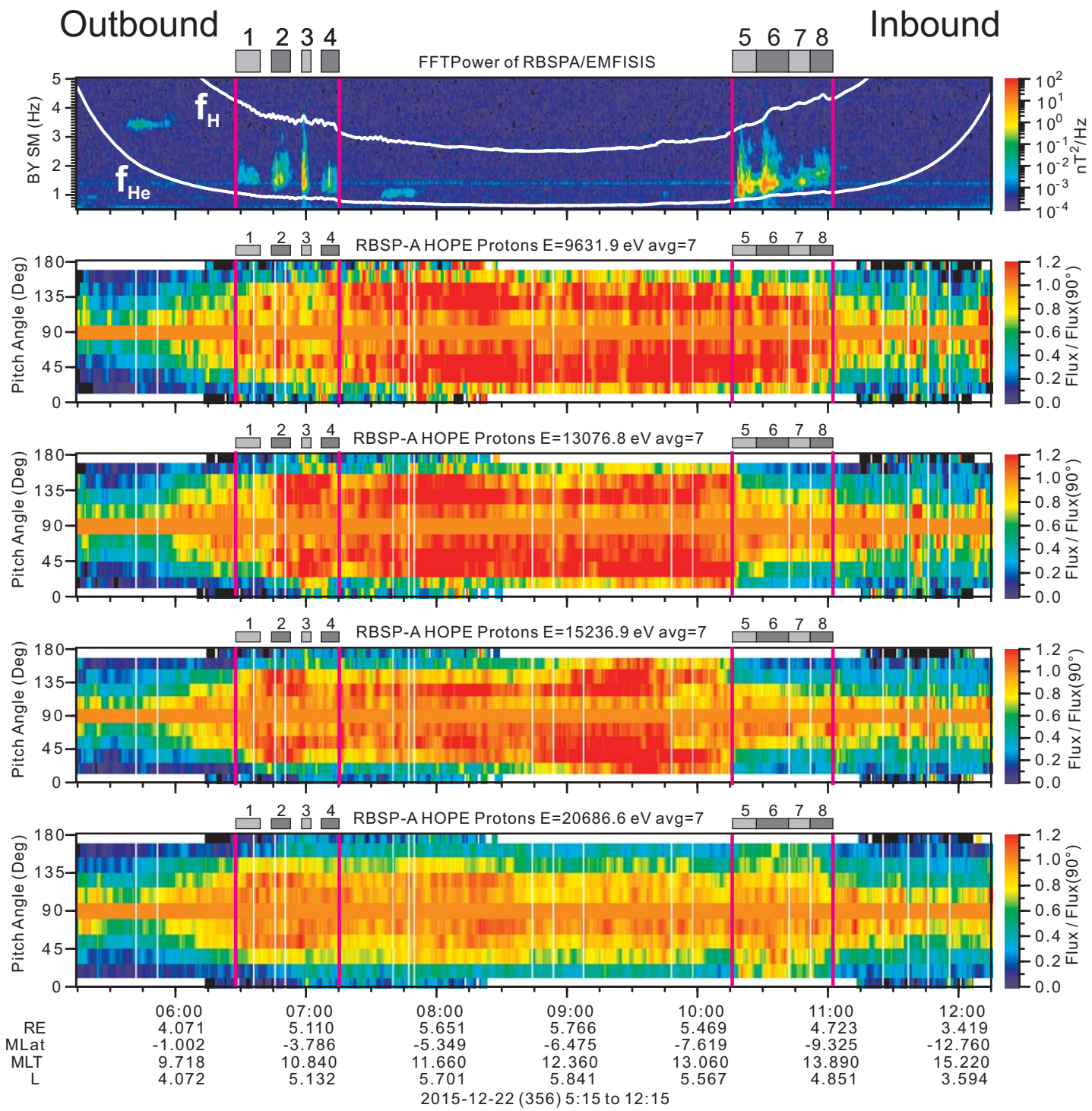
Outbound
Inbound
1 2 3 4
5 6 7 8
FFTPower of RBSPA/EMFISIS
BY SM (Hz)
f_H
f_{He}
nT²/Hz
RBSP-A HOPE Protons E=9631.9 eV avg=7
RBSP-A HOPE Protons E=13076.8 eV avg=7
RBSP-A HOPE Protons E=15236.9 eV avg=7
RBSP-A HOPE Protons E=20686.6 eV avg=7
Pitch Angle (Deg)
Flux / Flux(90°)
06:00 07:00 08:00 09:00 10:00 11:00 12:00
RE 4.071 5.110 5.651 5.766 5.469 4.723 3.419
MLat -1.002 -3.786 -5.349 -6.475 -7.619 -9.325 -12.760
MLT 9.718 10.840 11.660 12.360 13.060 13.890 15.220
L 4.072 5.132 5.701 5.841 5.567 4.851 3.594
2015-12-22 (356) 5:15 to 12:15

Figure 6

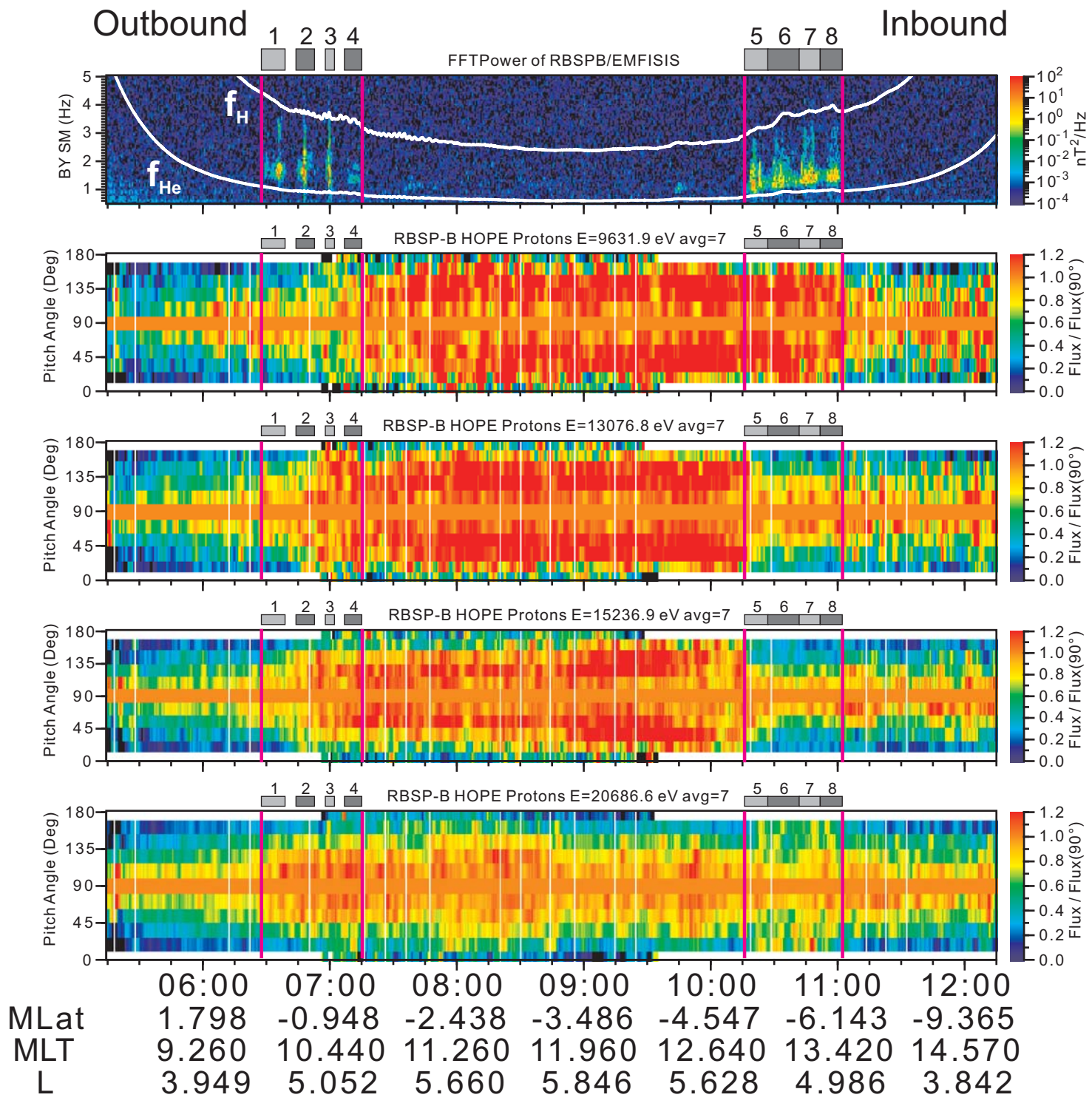

2015-12-22 (356) 5:15 to 12:15

Figure 7

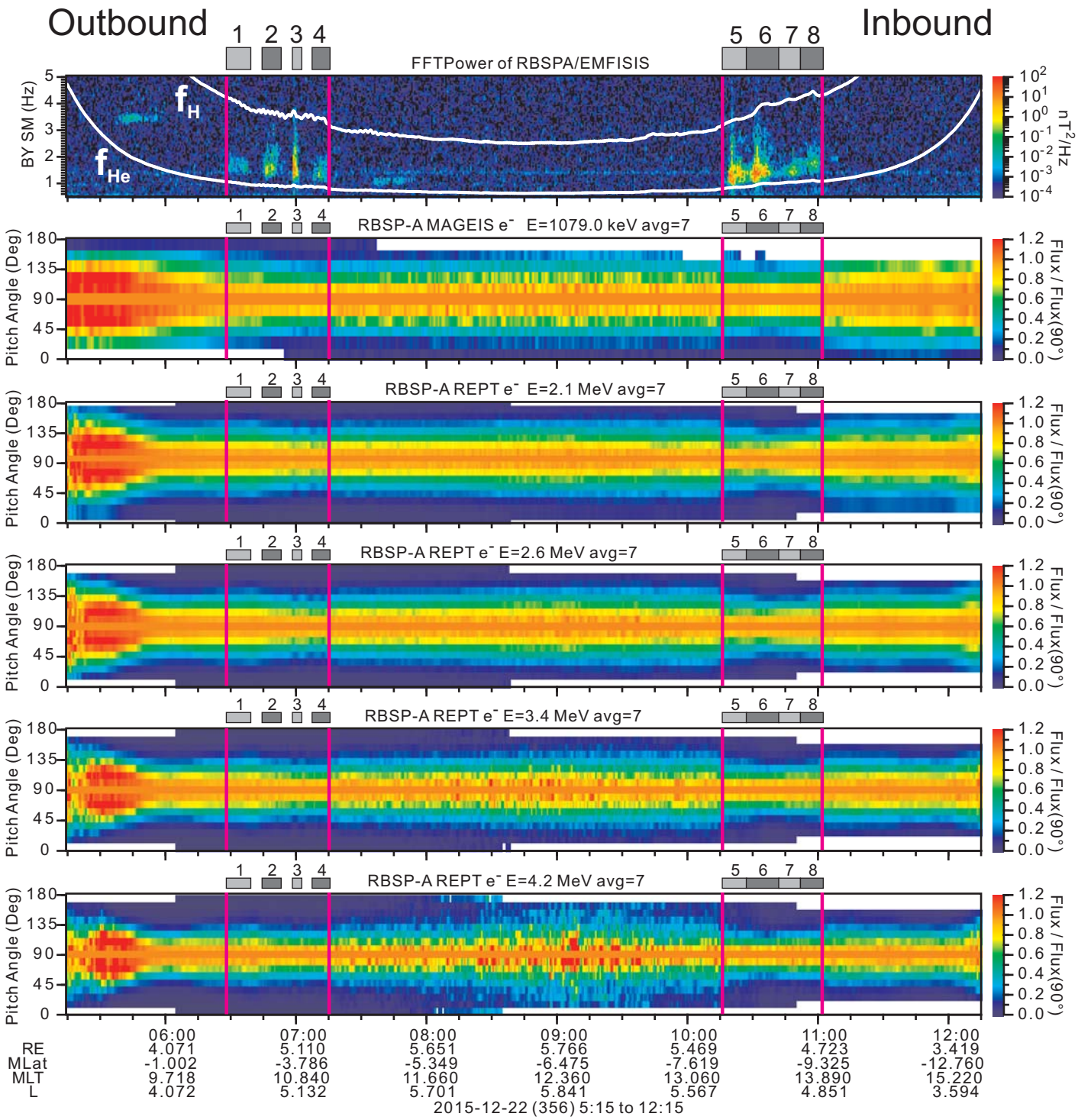
Outbound
Inbound
1 2 3 4
5 6 7 8
FFTPower of RBSPA/EMFISIS
BY SM (Hz)
f_H
f_{He}
nT²/Hz
RBSP-A MAGEIS e⁻ E=1079.0 keV avg=7
RBSP-A REPT e⁻ E=2.1 MeV avg=7
RBSP-A REPT e⁻ E=2.6 MeV avg=7
RBSP-A REPT e⁻ E=3.4 MeV avg=7
RBSP-A REPT e⁻ E=4.2 MeV avg=7
Pitch Angle (Deg)
Flux / Flux(90°)
RE
MLat
MLT
L
06:00 07:00 08:00 09:00 10:00 11:00 12:00
4.071 5.110 5.651 5.766 5.469 4.723 3.419
-1.002 -3.786 -5.349 -6.475 -7.619 -9.325 -12.760
9.718 10.840 11.660 12.360 13.060 13.890 15.220
4.072 5.132 5.701 5.841 5.567 4.851 3.594
2015-12-22 (356) 5:15 to 12:15

Figure 8

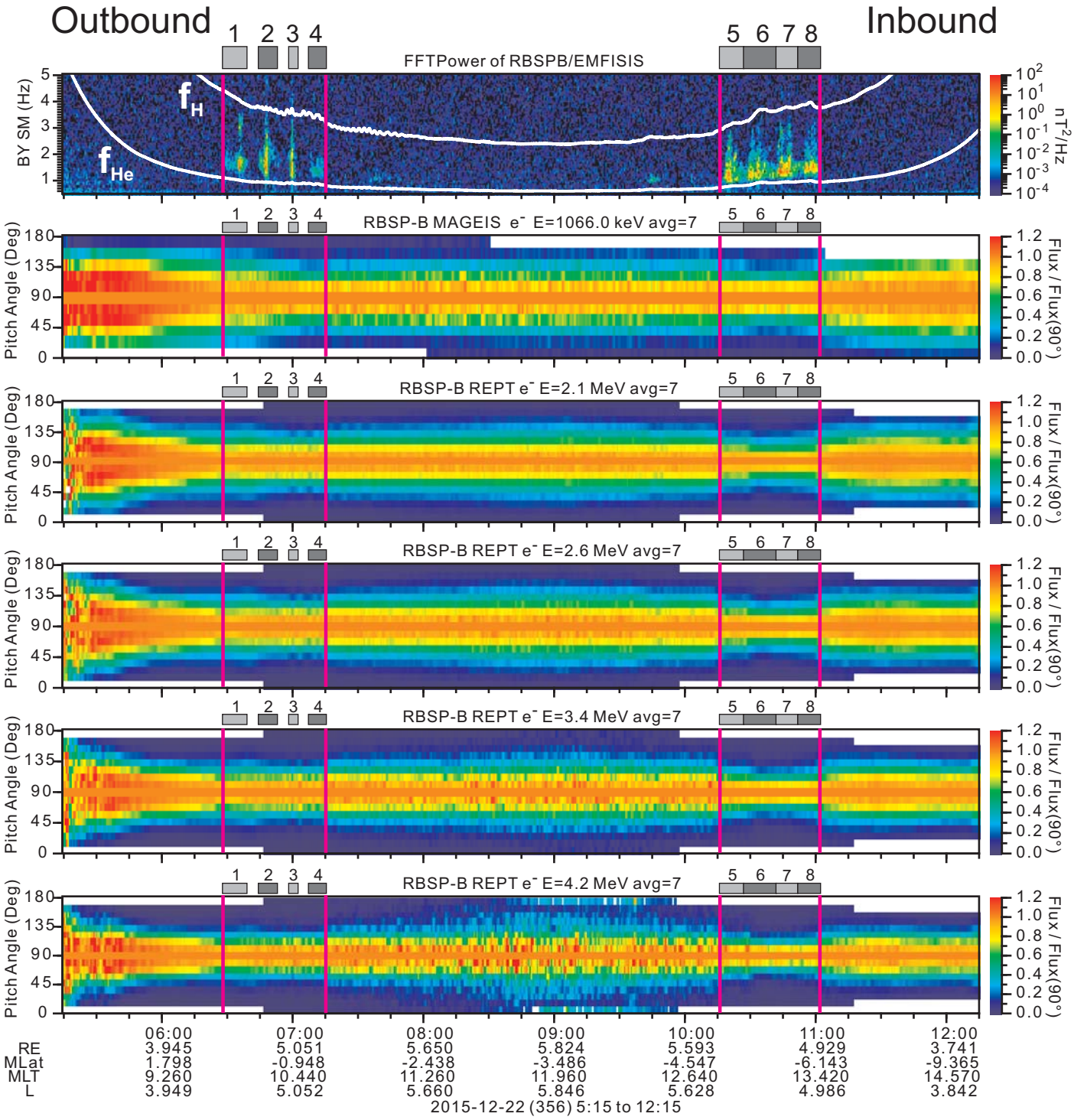
Outbound
Inbound
1 2 3 4
5 6 7 8
FFTPower of RBSPB/EMFISIS
BY SM (Hz)
f_H
f_{He}
nT²/Hz
RBSP-B MAGEIS e⁻ E=1066.0 keV avg=7
RBSP-B REPT e⁻ E=2.1 MeV avg=7
RBSP-B REPT e⁻ E=2.6 MeV avg=7
RBSP-B REPT e⁻ E=3.4 MeV avg=7
RBSP-B REPT e⁻ E=4.2 MeV avg=7
Pitch Angle (Deg)
Flux / Flux(90°)
RE
MLat
MLT
L
06:00 07:00 08:00 09:00 10:00 11:00 12:00
3.945 5.051 5.650 5.824 5.593 4.929 3.741
1.798 -0.948 -2.438 -3.486 -4.547 -6.143 -9.365
9.260 10.440 11.260 11.960 12.640 13.420 14.570
3.949 5.052 5.660 5.846 5.628 4.986 3.842
2015-12-22 (356) 5:15 to 12:15

Figure 9